remote sensing

MDPI

Article

Phenological Dynamics Characterization of Alignment Trees with Sentinel-2 Imagery: A Vegetation Indices Time Series Reconstruction Methodology Adapted to Urban Areas

Carlos Granero-Belinchon [1,*], Karine Adeline [1], Aude Lemonsu [2] and Xavier Briottet [1]

[1] ONERA-Department of Theoretical and Applied Optics, University of Toulouse, FR-31055 Toulouse, France; karine.adeline@onera.fr (K.A.); xavier.briottet@onera.fr (X.B.)

[2] Centre National de Recherches Météorologiques, Meteo-France-CNRS, FR-31057 Toulouse, France; aude.lemonsu@meteo.fr

* Correspondence: carlos.granero_belinchon@onera.fr

Received: 18 December 2019; Accepted: 11 February 2020; Published: 14 February 2020

Abstract: This article presents a novel methodology for the characterization of tree vegetation phenology, based on vegetation indices time series reconstruction and adapted to urban areas. The methodology is based on a pixel by pixel curve fitting classification, together with a subsequent Savitzky–Golay filtering of raw phenological curves from pixels classified as vegetation. Moreover, the new method is conceived to face specificities of urban environments such as: the high heterogeneity of impervious/natural elements, the 3D structure of the city inducing shadows, the restricted spatial extent of individual tree crowns and the strong biodiversity of urban vegetation. Three vegetation indices have been studied: Normalized Difference Vegetation Index (NDVI) and Normalized Difference Red Edge Index 1 (NDRE1), which are mainly linked to chlorophyll content and leaf density and Normalized Burn Ratio (NBR) mostly correlated to water content and leaf density. The methodology has been designed to allow the analysis of annual and intra-annual vegetation phenological dynamics. Then, different annual and intra-annual criteria for phenology characterization are proposed and criticized. To show the applicability of the methodology, this article focuses on Sentinel-2 (S-2) imagery covering 2018 and the study of groups of London planes in an alignment structure in the French city of Toulouse. Results showed that the new method allows the ability to (1) describe the heterogeneity of phenologies from London planes exposed to different environmental conditions (urban canyons, proximity with a source of water) and (2) to detect intra-annual phenological dynamics linked to changes in meteorological conditions.

Keywords: urban tree vegetation; phenology; time series reconstruction; Sentinel-2; NDVI; NBR; NDRE1

1. Introduction

The presence of vegetation improves the responsible and sustainable development of urban areas by offering several ecosystem services [1–3] such as: vegetation–climate interactions (air quality increase, urban cool island, rain water management and thermal comfort) [4,5], energetic consumption and CO2 track reductions [6], biodiversity conservation [6], human well-being [7], ambiance and socio-cultural benefits [7]. Among this urban vegetation, alignment trees create shade contributing to reduce the urban heat islands and fit the geometrical urban planning [8]. As an example in Paris, about 100,000 street trees cover around 700 km of roads and concern approximately 1600 roads out of 6000, inducing a shade covering about 3% of the city surface [9]. However, urban trees are exposed to increasing anthropic and climatic pressures [10,11]. Hence, monitoring their health is

essential to protect green areas in cities, anticipate changes in climatic forcing and guide environmental policies [12]. Ground surveys performed by members of the city hall departments managing the green areas of the city, or by external experts, have been traditionally used [13]. However, they are costly, require human resources and suffer a lack of high temporal repeatability to give an accurate report of health condition and its evolution. Remote sensing data is a good alternative and has been already largely used in urban environments for vegetation classification [14–19] and health assessment [20–23], with acquisitions from unmanned aerial vehicle sensors [15,24], airborne [14,20,25–27] and spaceborne sensors [16–18,28]. However, most of these previous studies work on a limited number of acquisitions along the year (often only one date) and as a consequence they cannot properly differentiate normal vegetation dynamics from a change in health condition.

Actually, vegetation dynamics are essentially controlled by the annual phenology, which depends on the climate seasonal variations determining key phases like greenup, maturity, senescence and dormancy periods and also depends on the biome type [29,30]. In addition, each vegetation species and individual has a specific phenology. Then, stress events can be detected by its intra-annual and/or inter-annual fluctuations. Studying vegetation phenology from remote sensing data requires a high temporal revisit, thus being mainly restricted to the use of satellite imagery. Thereafter, the term "phenology" frequently refers to the analysis of time series of spectral Vegetation Indices (VIs) computed from satellite images. The Normalized Difference Vegetation Index (NDVI) is the most used VI correlated to green leaf density (LAI), green biomass and green vegetation cover and has been historically obtained from AVHRR and MODIS sensors [29,31–34]. Although both of them take daily images, their spatial resolutions are coarse (NDVI is obtained at 500 m and 250 m, respectively), and only allow capturing the global phenology of vegetation communities from regional to national scale, but not at the local or individual scale needed in urban environments. On the other hand, other satellite sensors have a better spatial resolution such as the Landsat series (ground sample distance of 30 m), SPOT (10 m) and RapidEye (5 m) constellations, and with them more heterogeneous ecosystems can be studied [35,36]. However for Landsat sensors, the spatial resolution is still not adapted to urban tree crown dimensions and their lower temporal revisit of around 16 days considerably reduces the number of cloud free acquisitions to integrate for building the phenological curve [35]. The use of SPOT and RapidEye appears to be more adapted to study urban tree phenology with their higher temporal revisit between 1 and 5 days. However, their images are not freely available and this can represent a significant cost for accurate monitoring. Recently, new multi-spectral satellite sensors such as the European Sentinel-2 and the Israeli–French Venμs with a spatial resolution of 10/20 m and 10 m, and a temporal revisit of 5 and 2 days respectively, have the advantage to acquire information in a larger number of spectral bands (more than the traditional Red Green Blue (RGB) + Near InfraRed (NIR)). This opens the way to compute more VIs related to other vegetation bio-physico-chemical and structural variables of interest for tree health monitoring [37–41], for instance with leaf pigments content from the visible (VIS) and NIR spectral domains [42], and leaf water and dry matter content in the Short-Wave InfraRed (SWIR) domain [42].

In addition, VI time series from satellite imagery contain noise induced by atmospheric variability, cloud cover variability and illumination and observation geometries variability [43]. Consequently, dedicated techniques for noise reduction were developed and can be split into three different approaches: function fitting methods [44,45], harmonic analysis methods [46,47] and local filtering methods [48–50]. The first approach consists of fitting the measured VI time series with a fixed mathematical function, assuming that healthy vegetation phenology behaves as a given function of time. The main disadvantage is that this approach prevents us from observing possible intra-annual phenological dynamics. Several fixed functions have been tested: double logistic (D-L) function [51,52], double hyperbolic tangent (DHT) function [45] or assymetric Gaussian function [51]. Then, the harmonic analysis approach, based on modeling the VI curve by series of sines and cosines, hypothesizes a symmetrical behavior of phenology, and so is not able to capture asymmetrical phenological dynamics. Some methods belonging to this approach are: HANTS [53], Fourier Filtered

Cycle Similarity [47] or the Sellers et al. 1994 Fast Fourier Transform technique [54]. Finally, local filtering approach consists of time localized smoothing of the phenological curves constrained to some given hypotheses. Among the most used filters are the Savitzky–Golay (S-G) filter [50] and Best Index Slope Extraction (BISE) methods [48,49]. This last approach family allows us to observe asymmetries and intra-annual events, but the smoothing hypotheses should be well chosen. Finally, Vrieling et al. 2018 showed the importance of the number of available images to correctly characterize phenological dynamics with reconstruction methods (in their case D-L fitting) [45]. For instance, the performance of the phenology reconstruction methodology decreases when the number of available images decreases (for them from 27 to 15). In addition, they demonstrated that the distribution of the images across the year is also important, being necessary to sample greenup and senescence periods as well as minimal and maximal values (dormancy and maturity periods).

Previous studies characterizing the phenological dynamics of vegetation with the use of VIs derived from satellite imagery focus on natural (woodlands and wild areas) or agricultural environments [35,45,50–52], with urban environments remaining scarcely investigated [55–57]. In addition, they are mainly based on NDVI phenology curves [35,50–52] leaving the rest of VIs only slightly analyzed [45], and so, the spectral richness of new satellites is not fully taken into account. The lack of studies focused on the monitoring of urban tree phenological dynamics can be explained by the additional issues due to the specificities of urban environments such as: the high heterogeneity of impervious/natural elements and the high geometry variability of the city, as well as its 3D structure heterogeneity inducing shadow effects, the restricted spatial extent of individual tree crowns (around ten of meters) and the strong biodiversity of urban vegetation. Thus, studying phenology curves of urban vegetation, not only needs satellites with a high temporal resolution, but also satellites with high spatial resolutions (a few tens of meters). Nowadays, missions such as the European Sentinel-2 or the Israeli–French Venμs [58] seem to be appropriate for urban areas.

The objective of this article is to propose a new methodology adapted to urban areas to characterize tree phenology by using VI time series reconstruction from Sentinel-2 imagery. Globally, it is based on (1) a classification of vegetation pixels relying on phenological curve fitting, considering healthy tree phenology to approximately behave as a given fixed function and (2) the application of a filter on raw VI time series for pixels classified as vegetation. This methodology has been developed to successfully: face high heterogeneity of urban environments and shadows (challenge of mixed pixels), face atmospheric, cloud cover, illumination–observation geometry and registration variability between dates and characterize annual and intra-annual phenological dynamics. A first good study case to test the new method has been selected based on criteria such as the choice of mono-species trees (to avoid inter-species phenology variability which can hide or generate mixed phenological dynamics) with a large tree crown size (in the order of magnitude of the satellite spatial resolution) and in alignment structure (to facilitate the number of vegetation pixels). The London plane is a common deciduous broadleaf tree species in European cities like Brussels, London, Madrid and Toulouse, and its monitoring is extremely important since some trees have been sensitive to canker stain disease and dying for the last 70 years in Italy, France, United kingdom, Spain and Greece [59,60]. So, the study case for this article is focused on alignment London plane trees in the city of Toulouse, France, with a monitoring of their phenology over the year 2018 with Sentinel-2 imagery (2018 is the first complete year for which S-2 has a revisit of 5 days). For that purpose, different environmental conditions (urban canyons, the proximity with a source of water) for urban and peri-urban London planes are investigated to observe variations in phenological curves as described by three distinct VIs. The proposed methodology finally allows us to study both annual and intra-annual phenological characteristics. The second is defined as anomalous events in the global annual dynamic [35,61,62] possibly corresponding to stress/disturbance events when analyzed with meteorological information.

Section 2 describes the studied area, the satellite and climatological data used in the study. In Section 3, the proposed methodology is presented together with the annual and intra-annual criteria for phenology monitoring. Results are showed in Section 4 for the study case and the different

environment scenarios for the London plane trees. Section 5 discusses the appropriateness of the chosen hypotheses of the methodology formulation, the advantages and disadvantages of the criteria to characterize the phenology and the influences of meteorological factors on phenological curves. Finally, Section 6 presents conclusions and perspectives of this work.

2. Case Study and Data

2.1. Case Study

Toulouse is located in the south-west of France, close to the Pyrenees mountain range and between Atlantic ocean and Mediterranean sea. With around 500,000 inhabitants, it is the fourth largest city of the country. It is characterized by a humid temperate climate favoring vegetation development. Toulouse is crossed by the Garonne river and by the historical "Canal de Midi" and "Canal de Brienne" artificial canals. London planes are found in large avenues in the city center, but also along the river and the canals.

In this work, five different areas of Toulouse, where London planes can be found exposed to different environmental conditions, have been studied (see Figure 1):

(1) Canal de Brienne (Brienne): These old London planes are located near the city center and grow along a canal. The orientation of this alignment is north-west, with two rows of trees (one at each side of the canal) and crown widths between 10 and 20 m.
(2) Urban Canal de Midi (Midi Int): These London planes grow along a canal inside the city. The orientation of this alignment is mainly north, with two rows of trees (one at each side of the canal) and crown widths between 10 and 20 m.
(3) Peri-urban Canal de Midi (Midi Ext): Located outside the city, the orientation of this alignment presents small variations between north and west. It contains two rows of trees (one at each side of the canal) with crown widths between 10 and 20 m.
(4) Jules Guesde Avenue (JGuesde): Located in Toulouse city center, this alignment is oriented north-east. It contains between two and four rows of trees with crown widths between 5 and 10 m.
(5) Boulevard Francois Verdier-Boulevard Carnot-Boulevard Strasbourg (FVerdier): Located in the city center, the orientation of this alignment presents small variations between north and west. It contains between two and four rows with crown widths of about 10–15 m.

London planes from the city center (Brienne, Midi Int, JGuesde and FVerdier) are supposed to be exposed to pollution and high temperatures during summer due to the urban heat island effect [63], while London planes from Midi Ext do not. In addition, London planes from city center avenues (JGuesde and FVerdier) may be exposed to lack of water during droughts. This is not the case for London planes from the canals (Brienne, Midi Int and Midi Ext), which do not suffer from lack of water since water from canals moisten the soil under them, and in some cases roots reach directly the canal water. Furthermore, London planes from the canals (Brienne, Midi Int and Midi Ext) are rooted on wide soil surfaces, while planes from the city center avenues (JGuesde and FVerdier) are rooted on small soil squares surrounded by impervious materials such as asphalt or slabs (see Figure 1). At last, London planes from JGuesde also suffer from the impacts of their root system alteration and a soil replacement due to 2011–2013 road works in order to extend a tramway line (information from Town-Hall).

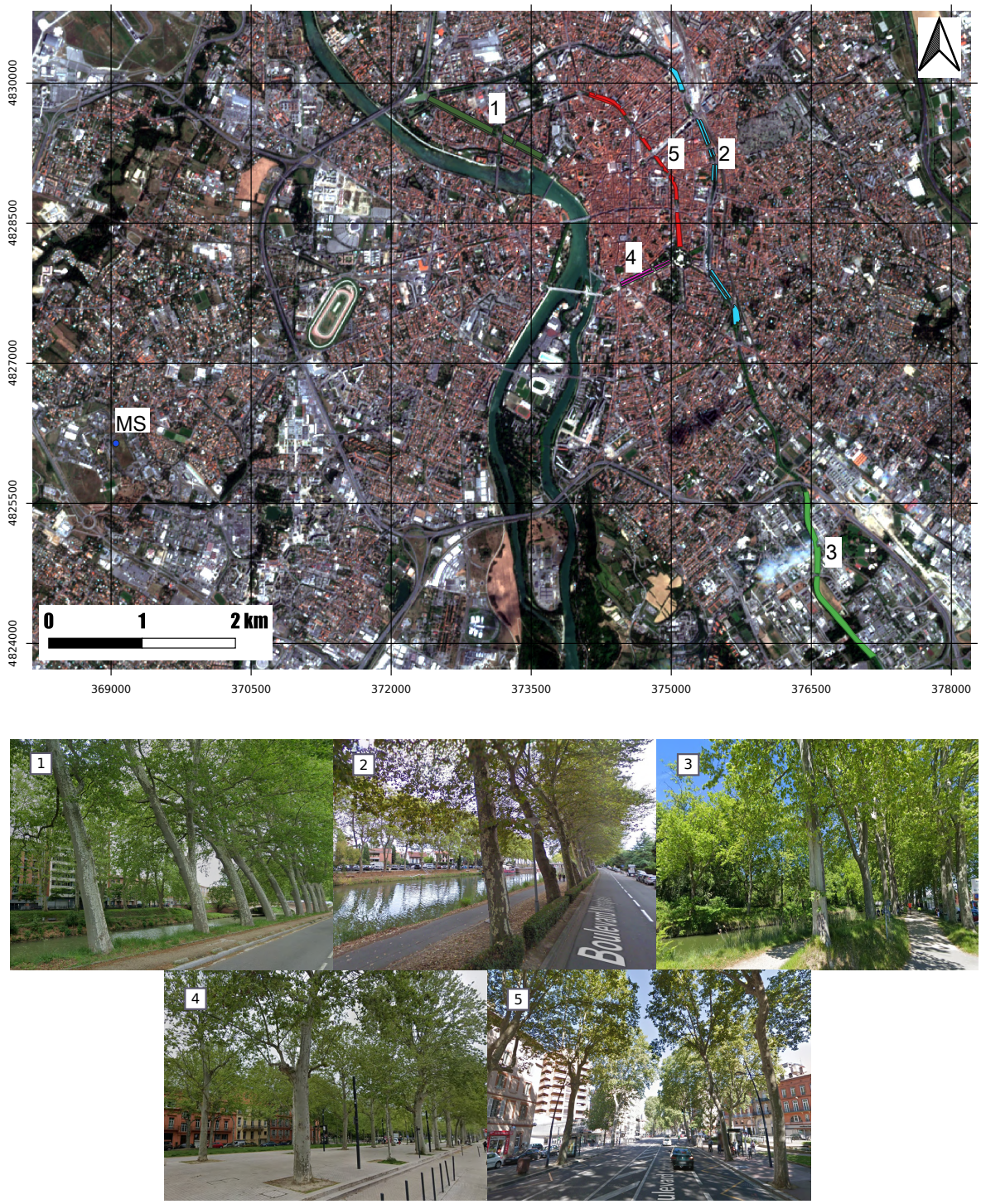

Figure 1. Above: Toulouse (France) Sentinel-2 Red Green Blue (RGB) composite image. The masked areas correspond to: (1) Canal de Brienne (dark green), (2) Urban Canal de Midi (Cyan), (3) Peri-urban Canal de Midi (light green), (4) J. Guesde Avenue (Magenta) and (5) F. Verdier Avenue (Red). The blue point with the label *MS* indicates the location of the meteorological station. Below: Google "Streetview" digital images from April 2019 (Brienne), May 2014 (MiDi Int), May 2019 (MiDi Ext), May 2015 (JGuesde) and July 2016 (FVerdier) are used to illustrate the sites.

2.2. Sentinel-2 and Meteorological Data: Toulouse (France) 2018

Sentinel-2 is a VNIR-SWIR multi-spectral European mission composed of two similar satellites Sentinel-2A and Sentinel-2B with 13 bands each. From the middle of 2017, when S-2B was launched

(S-2A was launched in June 2015), Sentinel-2 can provide one image of Toulouse every 5 days, with spatial resolutions of 10, 20 and 60 m depending on the spectral band, see Appendix A Table A1. In addition, the viewing angle of both Sentinel-2 satellites is almost constant across the year and very close to nadir (viewing zenithal angle $\theta_z^v \approx 3°$ and viewing azimuthal angle $\phi_a^v \approx 202°$). In Toulouse, the illumination angles (zenithal θ_z^i and azimuthal ϕ_a^i angles) at S-2 acquisition time (≈11:00 local time) varies along the year going from $\theta_z^i \approx 165°$ and $\phi_a^i \approx 65°$ during winter to $\theta_z^i \approx 145°$ and $\phi_a^i \approx 25°$ during summer, see Figure 2.

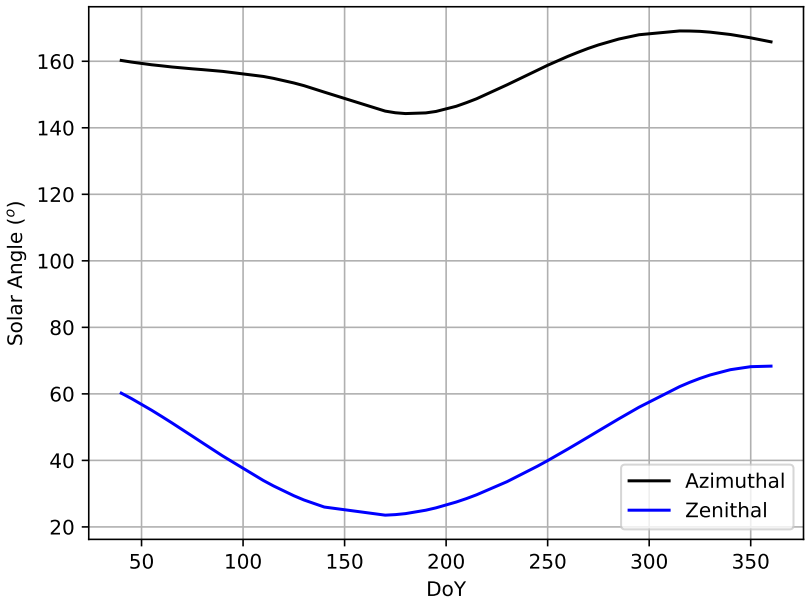

Figure 2. Toulouse (France) zenithal and azimuthal illumination angles at S-2 acquisition time (11:00) as a function of the Day of the Year (DoY).

THEIA platform (https:www.theia-land.fr) from CNES (Centre National d'Etudes Spatiaux (France)) gives free access to Sentinel-2 Bottom Of Atmosphere reflectance (level 2A) processed images of Toulouse. Moreover, THEIA provides co-registered images, with cloud masks, and quality and atmospheric information. For Sentinel-2A and Sentinel-2B combined products, the multi-temporal spatial registration performance varies between pixels, with approximately a third of pixels with co-registration errors of 0–50% of the pixel size, another third with errors around 100–150% of the pixel size, and the last third with errors in between [64]. For 2018, THEIA provides up to 37 S-2 images of Toulouse, among which there are 20 exploitable ones (images with strong cloud coverage, higher than 50% or hidden the studied areas, are not considered). These 20 exploitable images are distributed across the year in such a way that they sample both dormancy and maturity period, as well as greenup and senescence, thus allowing us to correctly apply phenology reconstruction methodologies.

Three VIs accessible with Sentinel-2 are studied in this work: NDVI and Normalized Difference Red Edge Index 1 (NDRE1) were considered to give information on leaf density and chlorophyll content [65] which are measured at 10 m and 20 m resolution respectively, and Normalized Burn Ratio (NBR), which is supposed to provide information on leaf density and water content [65] at 20 m resolution, see Table 1. Normalized indices are selected to facilitate quantification, comparison and description of phenological dynamics.

Table 1. Selected indices. Cab = Chlorophyll, LAI = Leaf Area Index, EWT = Water Content.

Variable	Index	Definition	Bands S-2	Spatial Resolution	Reference
LAI, Cab	NDVI-84	$\frac{\rho_{832}-\rho_{664}}{\rho_{832}+\rho_{664}}$	$\frac{b8-b4}{b8+b4}$	10 m	[65–67]
LAI, EWT	NBR	$\frac{\rho_{854}-\rho_{2200}}{\rho_{864}+\rho_{2200}}$	$\frac{b8-b12}{b8+b12}$	20 m	[65,68]
LAI, Cab	NDRE1	$\frac{\rho_{740}-\rho_{705}}{\rho_{740}+\rho_{705}}$	$\frac{b6-b5}{b6+b5}$	20 m	[69–71]

The meteorological data used over the year 2018 come from the Meteopole-Flux station installed on the Meteo France site 6.5 km south-west of the city center, see Figure 1. This permanent station has been operational since 2012 and allows the long-term monitoring of radiation and energy exchanges, meteorological variables and soil water and thermal status, for a grassland site on the outskirts of the Toulouse urban area. For this study, the data analyzed are the incoming short-wave radiation (in $W \cdot m^{-2}$) and the air temperature (in °C) recorded at 2 m above the ground, the soil water content (in $m^3 \cdot m^{-3}$) recorded by 16 sensors installed at different depths (from 10 to 220 cm depth) and precipitation (mm). Data are hourly available and are here post-processed to provide daily information of mean global incoming radiation, maximum temperature and cumulative precipitation. For water content, mean daily values are calculated by soil layers i.e., 10–50 cm, 50–100 cm and 100–220 cm, because the temporal dynamics of soil water status (especially its response to daily and subdaily precipitation) varies between near-surface layers and deep soil.

3. Methodology

3.1. Phenology Time Series Reconstruction

The proposed methodology presents four steps, see Figure 3.

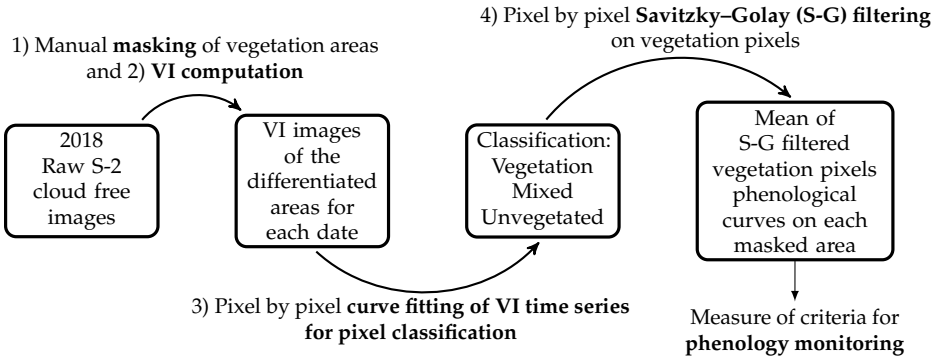

Figure 3. Proposed methodology for vegetation index (VI) phenological curve reconstruction.

(1) A manual masking aims at discriminating the vegetation study areas (in this study five masks are created, see Section 2.1). This mask is visually delineated by using S-2 images but also georeferenced open access airborne images of the city (Google Earth images). Only one mask per green studied area was used for the whole studied year. So, to entirely contain the vegetated area, the mask should be set during the period of the year for which vegetation occupies the largest area, both in terms of quantity of pixels and quantity of vegetation per pixel (this period usually corresponds to the maturity period). For this work, QGIS software was used to create the masks.

(2) The chosen VI was calculated for each pixel of the masked areas and for all the available dates of the year. Hence for each pixel, a raw VI time series, VI_t^0, with a number of samples equal to the number of available images, was obtained.

(3) Then, an unsupervised classification based on pixel by pixel weighted iterative fitting of phenological curves was applied. Weighted iterative curve fitting has been traditionally used to study vegetation phenology, by considering that healthy vegetation presents phenological curves

that can be described by fixed functions [45,51,52]. The proposed methodology takes advantage of this hypothesis and considers that pixels where the error fit is large are mixed or non-vegetated pixels. On the other hand, pixels where the error fit is considerably small, i.e., behaving as the imposed function, are considered vegetation pixels. In this work, double logistic function was chosen to describe phenology time series of VIs, since it presents less free parameters than the double hyperbolic tangent function and it has been shown to perform better than the asymmetric Gaussian function [51]. The double logistic function is expressed as:

$$VI(t) = VI_{min} + (VI_{max} - VI_{min}) \times \left(\frac{1}{1 + e^{-m_S(t-S)}} + \frac{1}{1 + e^{m_A(t-A)}} \right) \quad (1)$$

where VI_{min}, VI_{max}, S, A, m_S and m_A are the free parameters of the fit. With VI_{min} the minimum yearly value of the VI, VI_{max} its maximum yearly value, S the Day of the Year (DoY) indicating the inflection point when the curve raises (greenup period), A the DoY indicating the inflection point when the curve drops (senescence period) and m_S and m_A the slopes of the curve at days S and A respectively.

The weighted iterative process relies on the hypothesis that in urban environments, small co-registration errors between dates are the main source of noise induced on VI_t^0 time series, and thus, considers that sudden increases or drops of VI_t^0 values between dates are mainly due to changes in the fraction of vegetation within a pixel. To correctly characterize the vegetation phenology and reduce mixed pixels effect, more weight should be given to high VI values.

Then from a first fit (VI_t^1) of the pixel raw time series (VI_t^0), a set of weights are computed to give more prominence to high VIs values than to low ones (upper envelope of the curve):

$$W_{t_i} = \begin{cases} 1 & \text{if } VI_{t_i}^0 \geq VI_{t_i}^1 \\ 1 - \frac{d_{t_i}}{d_{max}} & \text{if } VI_{t_i}^0 < VI_{t_i}^1 \end{cases} \quad (2)$$

where W_{t_i} is the weight of sample at date t_i, VI_t^0 is the raw VI time series, VI_t^1 is the first fitted VI time series, $d_{t_i} = |VI_{t_i}^0 - VI_{t_i}^1|$ and $d_{max} = \max\left\{|VI_{t_i}^0 - VI_{t_i}^1|\right\} \forall i$.

Once the weights have been fixed from the first fitting, an iterative process starts until minimizing the fitting error defined as:

$$F_k = \sum_{i=1}^{N} (|VI_{t_i}^k - VI_{t_i}^0| \times W_{t_i}) \quad (3)$$

where F_k is the error at iteration k and N is the number of samples in the time series. Fits are performed with the Levenberg–Marquardt least squares method [72,73] of the SciPy library [74] for Python 3.6.

Finally, pixel classification is based on F_k errors and two thresholds, B_v and B_m. If $F_k < B_v$ then the pixel is considered as vegetated, if $B_v \leq F_k < B_m$ the pixel is considered as mixed and if $F_k > B_m$ the pixel is considered as not (or poorly) vegetated. B_v and B_m were empirically chosen to be respectively 5% and 10% of the annual maximal value VI of the pixel. For our study case, these bounds appear strict enough to importantly reduce non-vegetated pixels in those classified as vegetation. An additional condition was applied: among the pixels initially classified as vegetation on each masked area, only pixels whose mean VI value during the maturity period is comprised within one standard deviation (std) of the ensemble of vegetation pixels over the same period, were retained. For London planes in Toulouse, we defined this period between 1st of May and 1st of October, since for this species in Toulouse, greenup and senescence periods correspond to the beginning of spring and the beginning of autumn respectively. Background effects are major during winter (when there are no leaves) and during the start of the greenup

period and the end of the senescence period. So, the choice of the maturity period bounds were done considering that from 1st of May to 1st of October the vegetation cover should be enough to minimize the influences of ground in the statistical measures. Adding this condition on the mean VI values allows us to avoid, as much as possible, false-positives in the classification.

(4) A weighted iterative Savitzky–Golay filtering was applied on vegetation pixels as classified in step (3). It allows us to reduce the noise that registration variability between dates induces on time series, and as it does not fix the phenological behavior, it allows us to observe intra-annual periods of disturbance and anomalies in vegetation phenological curves. The weighted iterative Savitzky–Golay filter used in this work is our own implementation (in Python 3.6) of the filter presented in Chen et al. 2004 [50], but it was adapted to process not uniformly sampled time series. Savitzky–Golay filter presents two free parameters: the width of the smoothing window (m) and the degree of the fitting polynomial (d).

   (a) First, an automatic search of the best parameter values within a given range, $m \in [6, 10]$ and $d \in [2, 4]$, was done [50]. These ranges were fixed following [50] and considering the number of available dates. On one hand, too small m values may lead to an over-fit of the raw VI time series, and so, difficulties can raise in capturing long-term trends. However, too large m values may lead to neglecting some important variations in the phenological curve. On the other hand, small values of d may lead to smoother results, and large values of d may over-fit the raw VI time series and generate noisy results. In addition, to perform a polynomial fit, the degree d of the polynomial must be lower than the size m of the smoothing window.

   (b) Then, once the first filtering was performed providing $VI_{t_i}^{1,\text{filt}}$, weights were assigned following the same hypothesis as in Equation (2), and a new VI time series ($VI_t^{1,ts}$) is:

$$VI_{t_i}^{1,ts} = \begin{cases} VI_{t_i}^{0} & \text{if } VI_{t_i}^{0} \geq VI_{t_i}^{1,\text{filt}} \\ VI_{t_i}^{1,\text{filt}} & \text{if } VI_{t_i}^{0} < VI_{t_i}^{1,\text{filt}} \end{cases} \tag{4}$$

   where "filt" indicates filtered signal, and "ts" indicates built VI time series.

   (c) Savitzky–Golay is applied iteratively on the new obtained VI time series ($VI^{1,\text{ts}}$) with smaller smoothing window size ($m = 6$) and greater polynomial order ($d = 4$). The iterative process searches at minimizing the error defined such as in Equation (3).

From step (3), another characterization of vegetation health status can be directly obtained from the D-L fitted curves of pixels classified as vegetation. Thus in Section 4.3, this alternative methodology is compared to the proposed one. However, D-L fitting characterization does not allow us to describe intra-annual dynamics and is then not advised. On the contrary, the proposed methodology by using S-G filtering does not fix a given behavior for the phenological curve and then it allows us to reduce VI time series noise without masking intra-annual anomalies in the phenological dynamics. So, annual and intra-annual dynamics can be studied, see Sections 3.2 and 3.3.

3.2. Annual Phenology Characterization

The final VI time series obtained from the previous reconstruction methodology should be analyzed by looking at different phenological information that can be compared from one year to another [45]:

(a) VI_{max} : The maximum value of the VI reached during the year, see Figure 4.

(b) $\text{Green}_{\text{period}}$: Normalized area under the curve during the maturity period (defined from 1st of May to 1st of October), see Figure 4. Measured areas are normalized with respect to the maximal possible VI area in this period. For normalized VIs (such as NDVI, NDRE1 and NBR), the maximal possible area is equal to the area under the unity-valued square-shaped function

between 1st of May and 1st of October. Thus, the measure is equivalent to a mean VI value for the maturity period.

(c) SOS20 (Start Of Season), SOS50, $PS90_S$ (Peak Season): Days of the year at which the VI amplitude is, respectively, 20%, 50% and 90% of the maximum amplitude, during the spring/summer period, i.e., the greenup period, see Figure 4.

(d) EOS20 (End Of Season), EOS50, $PS90_E$: Days of the year at which the VI amplitude is, respectively, 20%, 50% and 90% of the maximum amplitude, during the summer/fall period, i.e., the vegetation senescence period, see Figure 4.

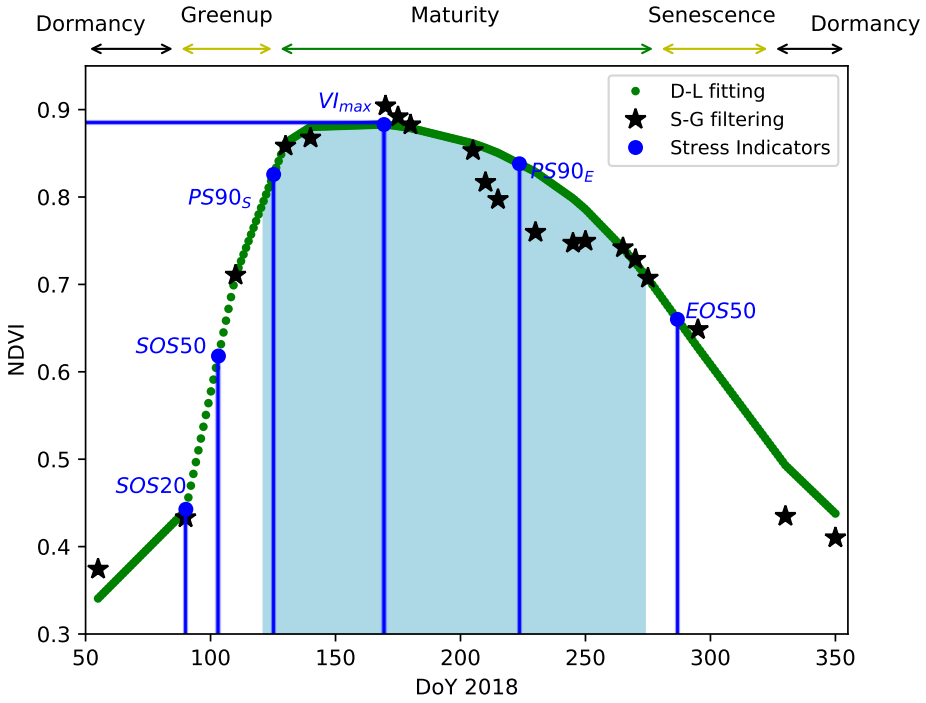

Figure 4. Phenological curve as described by Normalized Difference Vegetation Index (NDVI) (Double logistic approximation in green and Savitzky–Golay filtering in black) and annual phenological characterization criteria (blue), $Green_{period}$ area is colored in light blue for clarity. Case study of Canal de Brienne area, Toulouse, 2018. Main vegetation phenological periods are outlined in the top of the figure: Dormancy, Greenup, Maturity and Senescence [44].

3.3. Intra-Annual Phenology Characterization

The S-G reconstruction methodology allows us to observe intra-annual dynamics, that might be related to phenological disturbance periods during the year. Here, these periods are defined as periods with anomalous dynamics (that are unpredictable with reconstruction methods imposing a function behavior): periods where the concavity/convexity of the phenological curve is suddenly broken [35,61,62]. Their quantification can be assessed with:

(e) $SlVI_{t_i}$: Negative slope (VI/day) of the VI curve at the beginning of the phenological disturbance period, see Figure 5. This indicator provides information on the strength of the perturbation. The more negative the slope is, the more important the phenological disturbance is, i.e., the more important is the concavity break.

(f) DiffA: Normalized area between the phenological curve and the straight line joining the start and the end of the phenological disturbance period, see Figure 5. Normalization is applied over the number of days corresponding to the phenological disturbance period. This straight line is assumed to be the lower possible bound of a non-disturbed phenological curve. This indicator

not only provides information on the importance of the perturbation but also on the capacity of the vegetation to restore.

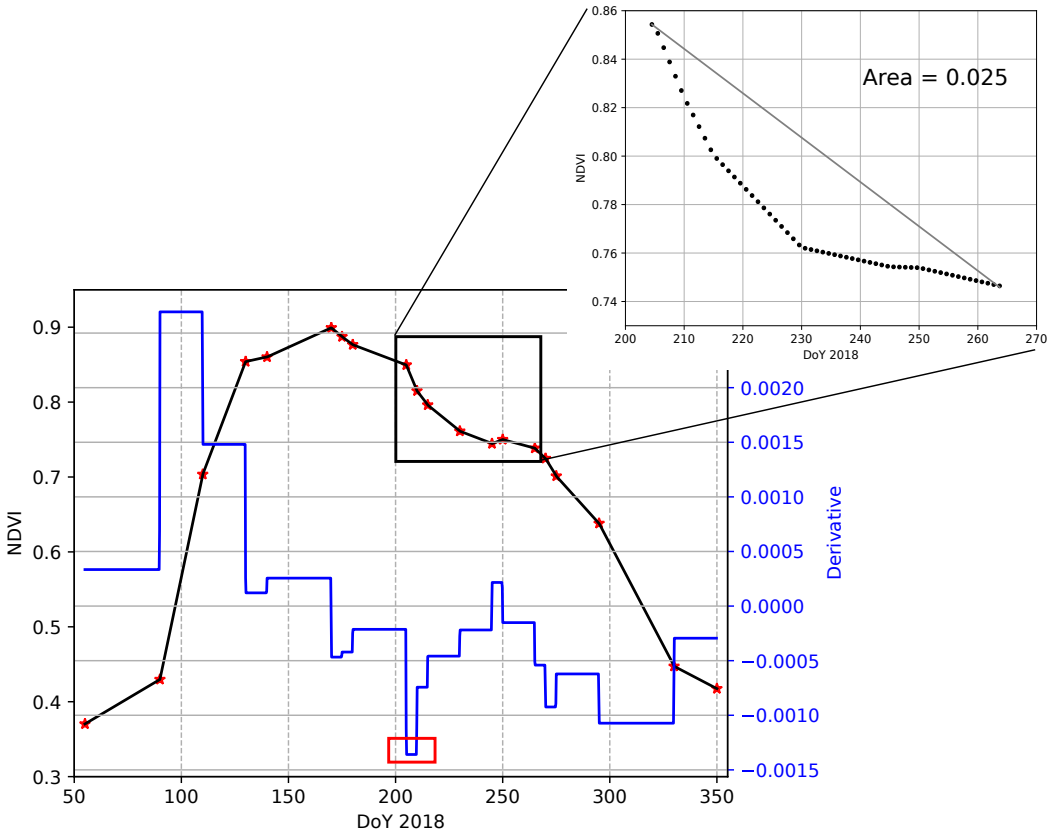

Figure 5. Phenological curve as described by NDVI in black and its derivative ($SlVI_{t_i}$) in blue. DiffA is also shown in the zoomed image. The value of $SlVI_{t_i}$ at the beginning of the phenological disturbance period is surrounded by the red rectangle. Case study of Canal de Brienne area, Toulouse, 2018.

On a global overview of the chosen annual criteria, vegetation phenology is analyzed through the maximum values of the VI (VI_{max}), but also, by studying how long vegetation maintains high VI values ($Green_{period}$, $PS90_S$, $PS90_E$), how fast is greenup (SOS20,SOS50) or when senescence arrives (EOS20, EOS50). Two additional criteria are also proposed to quantify intra-annual anomalous phenology events ($slVI_{t_i}$ and DiffA).

4. Results

This section studies the performances of the above presented methodology when it was applied to characterize urban and peri-urban London plane phenological curves as described by NDVI, NBR and NDRE1, see Table 1. First, the performances of the pixel classification and the S-G filtering steps are shown. Then, the reconstructed time series are used to characterize the vegetation phenological dynamics. The results obtained with the S-G filtered time series are compared to those obtained with a fitting function (double logistic) time series reconstruction method applied on the pixels classified as vegetation. Only pixels in the masked areas shown in Figure 1 are processed.

4.1. Classification of Vegetation Pixels

Figure 6 shows the classification map obtained with curve fitting on the Canal de Brienne area, with NDVI (10 m resolution), NBR (20 m resolution) and NDRE1 (20 m resolution) respectively. Based on step (3) of the methodology described in Section 3.1, vegetation pixels are colored in fuchsia, mixed pixels in cyan and non-vegetation pixels in blue. As expected, the number of vegetation pixels is higher with NDVI than with NBR or NDRE1 due to the difference in spatial resolution. Further, the location of the vegetation pixels at 20 m overlaps that of the vegetation pixels at 10 m. However, vegetation pixel locations from NBR and NDRE1 do not fully coincide. Figure 7 shows the raw VI curves for pixels classified as vegetation on the five studied areas for NDVI, NBR and NDRE1. After classification, pixels classified as vegetation present a common phenology behavior associated to vegetation in any of the studied sites. In addition, whatever the indices, the differences of the VI values between time series are smaller on Brienne, Midi Int and Midi Ext compared to JGuesde and FVerdier sites. A larger range of VIs value variations during the winter season is also noticed, whatever the location, but being larger in FVerdier. This effect is due to the background heterogeneity, since during the dormancy period, the lack of leaves increases the background influences on the phenological curve.

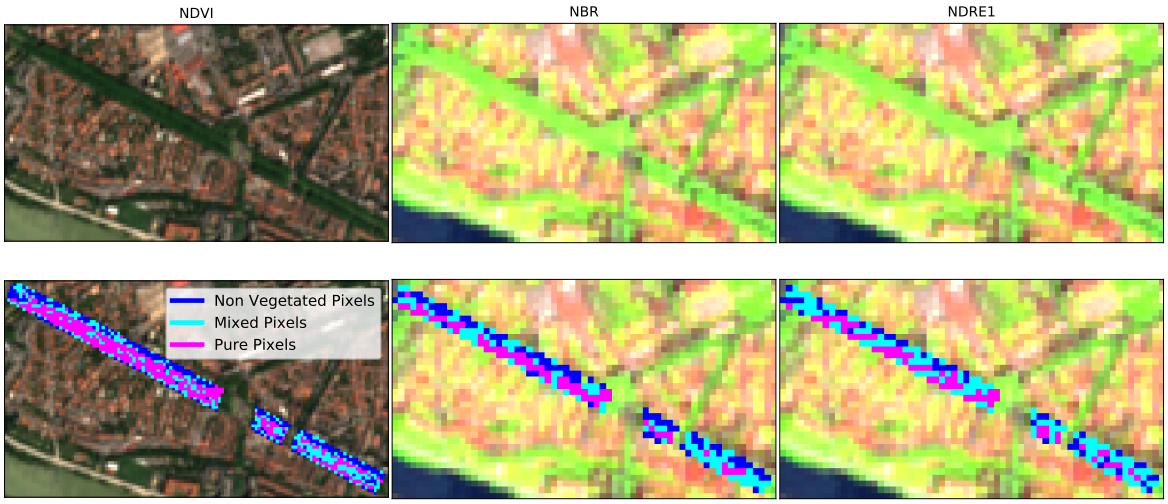

Figure 6. The 2018 London plane classification map obtained by applying the proposed methodology with NDVI (**left**) at 10 m resolution, Normalized Burn Ratio (NBR) (center) at 20 m resolution and Normalized Difference Red Edge Index 1 (NDRE1) (**right**) at 20 m resolution for Canal de Brienne area. Fuchsia indicates vegetation pixels, cyan indicates mixed pixels with an important quantity of vegetation while blue indicates non-vegetation pixels. Background are the RGB (**left**) and B6-B8A-B12 (**center** and **right**) composite Sentinel-2 images for 25th July 2018.

Table 2 shows the number of pixels classified as vegetation together with the percentage they represent in each studied area. It also shows, for each studied site, the standard deviation of the VI values of the vegetation pixels during the maturity period. For every VI, Brienne and Midi Ext present the lowest standard deviations (between 0.02 and 0.03 depending on the VI), followed by Midi Int (0.03, 0.04 and 0.05 for NDVI, NBR and NDRE1 respectively). For NDVI, the percentage of vegetation pixels is higher for Brienne and Midi Ext than over the other sites. On the other hand, for both NBR and NDRE1 the highest percentages of vegetation pixels are found for Midi Ext and JGuesde. Moreover, the percentage of pixels classified as vegetation obtained for the studied areas is more regular with NDRE1 (between 29% and 40% of pixels), while for NDVI and NBR larger variations are found (between 22% and 58% for NDVI and 13% and 46% for NBR). This can indicate that D-L fitting classification with NDRE1 is less influenced by the type of background.

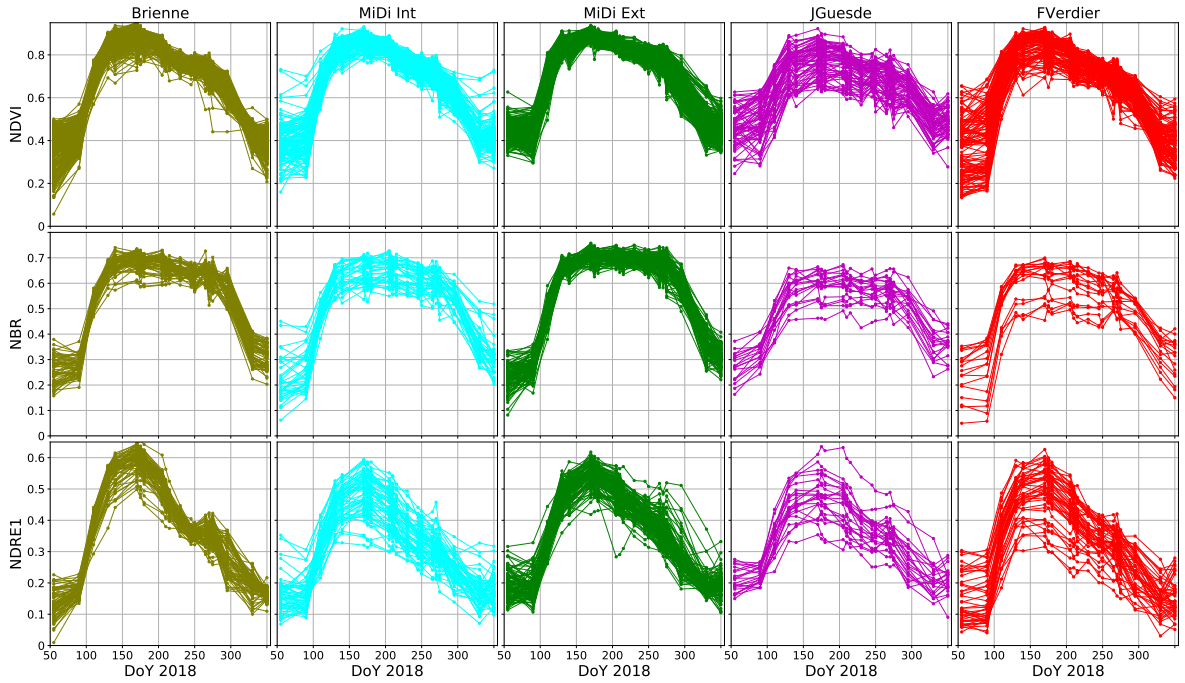

Figure 7. The 2018 London plane raw phenological curves for pixels classified as vegetation with NDVI (**top**), NBR (**center**) and NDRE1 (**bottom**) for the five studied sites from left to right: Brienne, Midi Int, Midi Ext, JGuesde and FVerdier.

Table 2. Curve fitting classification performances for NDVI, NBR and NDRE1. # indicate the number of pixels and "std" the standard deviation of the VI values of the vegetation pixels during the maturity period.

	NDVI			**NBR**			**NDRE1**		
	# pixels	**# vegetation**	**std**	**# pixels**	**# vegetation**	**std**	**# pixels**	**# vegetation**	**std**
Brienne	918	379 (41.2%)	0.02	229	66 (28.8%)	0.03	229	68 (29.7%)	0.03
MiDi Int	654	143 (21.8%)	0.03	154	41 (26.6%)	0.04	154	55 (35.7%)	0.05
MiDi Ext	1041	610 (58.5%)	0.02	257	120 (46.7%)	0.02	257	103 (40.0%)	0.03
JGuesde	219	70 (31.9%)	0.06	54	20 (37.0%)	0.05	54	22 (40.7%)	0.06
FVerdier	564	129 (22.8%)	0.04	145	20 (13.7%)	0.06	145	45 (31.0%)	0.06

4.2. Savitzky–Golay Filtering to Build Vi Time Series

Figure 8 allows to compare the NDVI (a), NBR (b) and NDRE1 (c) Savitzky–Golay filtered time series for pixels from Canal de Brienne classified as vegetation, mixed and non-vegetation pixels. Green lines represent pixels that are completely occupied by London planes. They show the highest VI values and after application of the proposed methodology, no sudden variability between dates remains. They also exhibit the smallest standard deviation. Black lines represent non-vegetated (or very few vegetated, or very unhealthy vegetation) pixels. They show the lowest VI values and, after applying the proposed methodology, noise remains important. This can be due to misregistration between dates, i.e., the composition of the pixels varies from one date to another, sometimes partially containing vegetation. In between, yellow line represents mixed pixels, with variable vegetation proportion. It can also represent unhealthy vegetation pixels, i.e., pixels for which the phenology curve can not be fitted by a given fixed function such as "double logistic" or "double hyperbolic tangent". Both, mixed and non-vegetated pixels present large standard deviations showing the existence of very different phenology behaviors in these groups. However, Figure 8 shows that the yellow means are very close to the green ones with a very similar behavior. This may indicate that the classification procedure has

been restrictive. This strict classification is used to avoid false-positive vegetation pixels in the analysis. Identical qualitative results are found for the other studied areas (data not shown).

Figure 8 also shows, in red, the mean of the D-L fitted curve for vegetation pixels. While for NBR green and red curves are very similar, for NDVI and NDRE1 the red line does not describe the drop appearing for the green one at $DoY \approx 205$. In addition, D-L fitting, imposing a fixed function, provides smoother VIs time series, as expected.

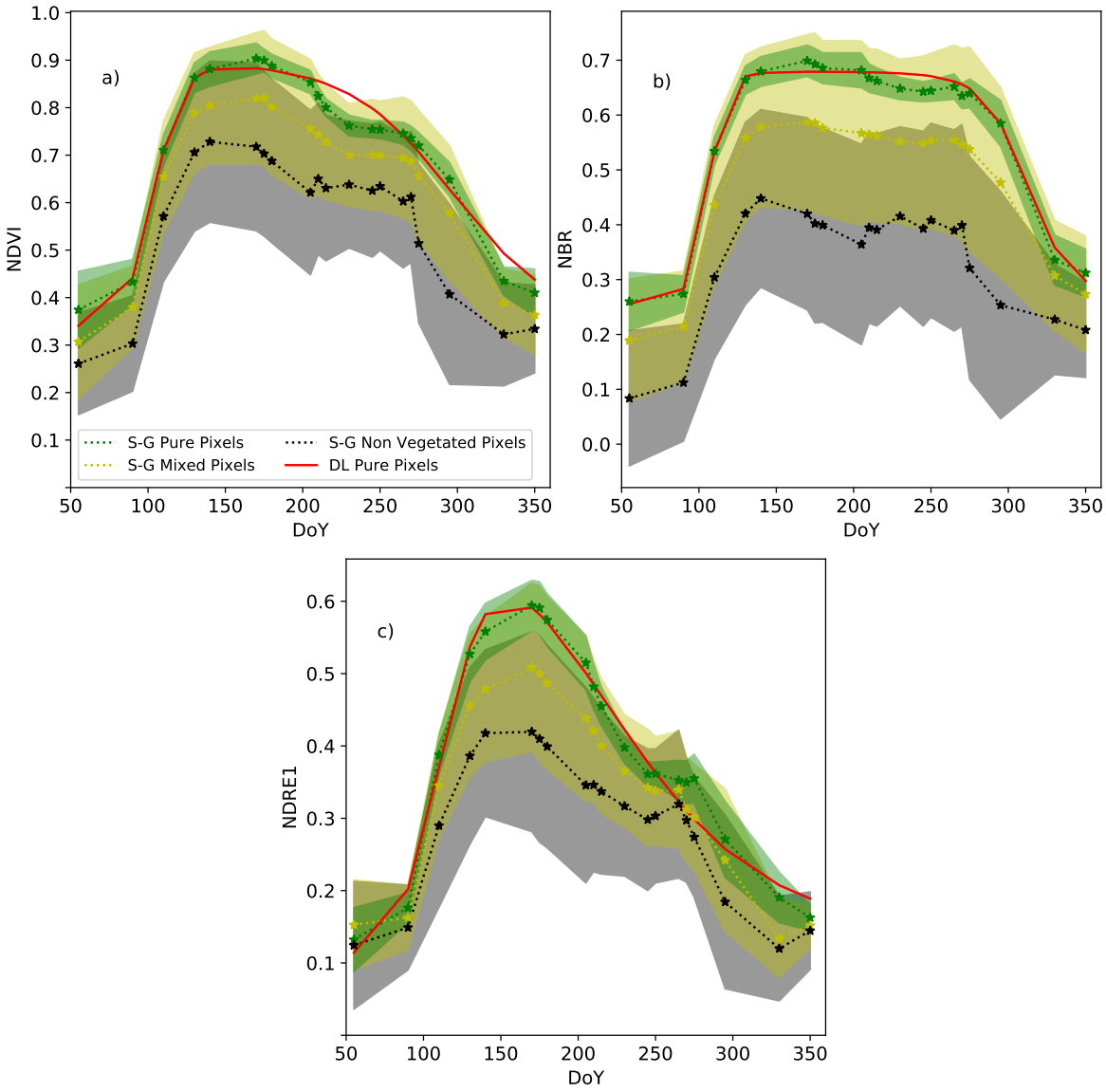

Figure 8. Savitzky–Golay reconstruction of the 2018 phenological curves as described by NDVI (**a**), NBR (**b**) and NDRE1 (**c**) for Canal de Brienne area and for vegetation pixels in green, mixed pixels in yellow and non-vegetated pixels in black. Dashed lines and stars represent the mean of VI time series and the area around represent the standard deviation. The red continuous curve represents the mean behavior of D-L fits on vegetation pixels.

4.3. Analysis of Phenological Dynamics from Vi Time Series

4.3.1. Annual Dynamics

Two methodologies to reconstruct vegetation phenological curves are compared in this section: Savitzky–Golay filtering and double logistic fitting, both applied on pixels previously classified as vegetation.

Figure 9 shows the phenology curves of London planes as characterized by NDVI (a, b), NBR (c, d) and NDRE1 (e, f) for the five studied areas described in Section 2.1. Curves in left column of Figure 9 are defined as the mean of the Savitzky–Golay filtered phenology curves, while curves in right column of Figure 9 are defined as the mean of the double logistic fitted phenology curves. In Figure 9a–d differences between the five sites can be observed with the NDVI and NBR reconstructed time series, and independently of the reconstruction methodology. These differences are quantified by VI_{max}, and $\text{Green}_{\text{period}}$ criteria, see Tables 3 and 4 for S-G and D-L methods respectively. Both methods show that London planes along the artificial canals present the highest values in NDVI and NBR, with peri-urban London planes from Canal de Midi (Midi Ext) presenting the highest values: $NDVI_{max}^{S\text{-}G} = 0.90 \pm 0.01$ and $NBR_{max}^{S\text{-}G} = 0.72 \pm 0.02$. On the other hand, London planes from the avenues (F.Verdier and J.Guesde) exhibit smaller NDVI and NBR values. Indeed, London planes from J. Guesde avenue, with $NDVI_{max}^{S\text{-}G} = 0.77 \pm 0.10$ and $NBR_{max}^{S\text{-}G} = 0.58 \pm 0.14$, have the lowest values during the maturity period. This is not the case for NDRE1 reconstructed time series (Figure 9e,f), for which Brienne and Midi Ext present the highest NDRE1 values (for Brienne London planes $NDRE1_{max}^{S\text{-}G} = 0.60 \pm 0.03$), with the other three sites showing lower values during the maturity period ($NDRE1_{max}^{S\text{-}G} = 0.49 \pm 0.06$ for Midi Int, $NDRE1_{max}^{S\text{-}G} = 0.50 \pm 0.07$ for FVerdier and $NDRE1_{max}^{S\text{-}G} = 0.48 \pm 0.06$ for JGuesde).

Table 3. Mean of the annual phenological dynamics criteria on S-G filtered phenological curves for NDVI, NBR and NDRE1 and for the five studied areas. Standard deviations are indicated within brackets.

NDVI	**SOS20 (DoY)**	**SOS50**	**PS90$_S$**	**PS90$_E$**	**EOS50 (DoY)**	**VI_{max} (VI)**	**$\text{Green}_{\text{period}}$ (%)**
Brienne	93 (4)	106 (7)	140 (21)	201 (6)	290 (11)	0.90 (0.05)	82 (5)
MiDi Int	95 (4)	108 (3)	144 (20)	202 (9)	285 (10)	0.88 (0.03)	80 (3)
MiDi Ext	97 (4)	110 (3)	142 (17)	202 (6)	290 (6)	0.90 (0.01)	84 (2)
JGuesde	91 (14)	112 (11)	154 (22)	210 (16)	290 (15)	0.77 (0.10)	72 (11)
FVerdier	92 (7)	105 (8)	150 (28)	200 (10)	289 (13)	0.85 (0.09)	78 (9)
NBR	**SOS20 (DoY)**	**SOS50**	**PS90$_S$**	**PS90$_E$**	**EOS50 (DoY)**	**VI_{max} (VI)**	**$\text{Green}_{\text{period}}$ (%)**
Brienne	95 (2)	105 (2)	136 (16)	221 (20)	304 (7)	0.69 (0.06)	65 (6)
MiDi Int	94 (3)	107 (3)	136 (14)	229 (22)	304 (7)	0.65 (0.05)	61 (6)
MiDi Ext	95 (3)	108 (3)	137 (12)	251 (27)	306 (5)	0.72 (0.02)	68 (2)
JGuesde	89 (7)	110 (11)	146 (17)	251 (36)	305 (9)	0.58 (0.14)	54 (15)
FVerdier	94 (4)	104 (3)	133 (14)	222 (23)	297 (11)	0.59 (0.12)	55 (12)
NDRE1	**SOS20 (DoY)**	**SOS50**	**PS90$_S$**	**PS90$_E$**	**EOS50 (DoY)**	**VI_{max} (VI)**	**$\text{Green}_{\text{period}}$ (%)**
Brienne	94 (3)	108 (3)	165 (24)	196 (3)	244 (16)	0.60 (0.03)	48 (2)
MiDi Int	96 (8)	112 (5)	159 (21)	198 (5)	256 (15)	0.49 (0.06)	41 (5)
MiDi Ext	97 (7)	115 (8)	158 (18)	200 (10)	269 (13)	0.55 (0.03)	47 (3)
JGuesde	96 (3)	110 (5)	153 (20)	205 (14)	263 (24)	0.48 (0.06)	42 (5)
FVerdier	96 (2)	107 (3)	166 (23)	199 (9)	260 (16)	0.50 (0.07)	41 (6)

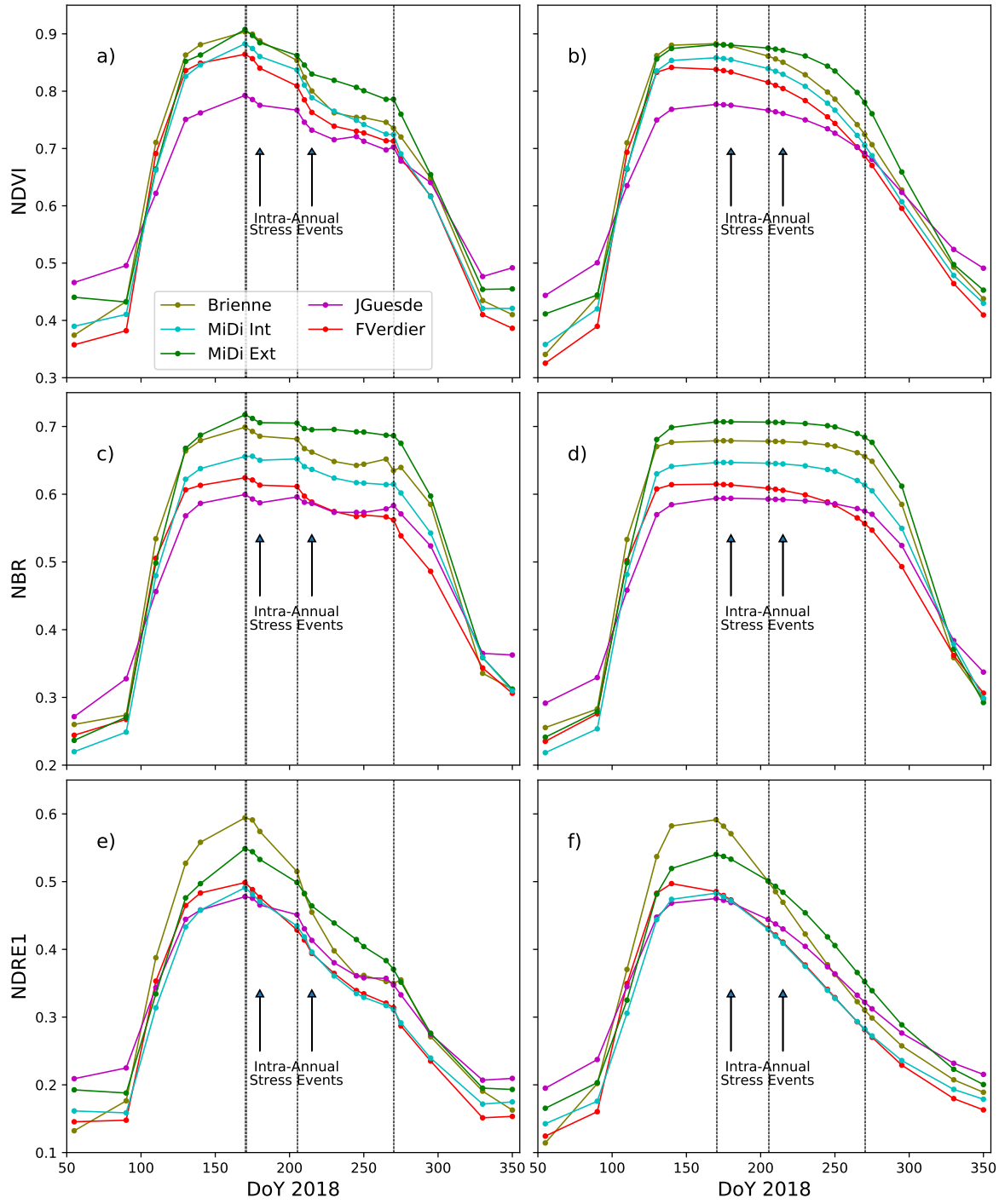

Figure 9. Reconstruction of the 2018 London plane phenological curves with Savitzky–Golay filtering as described by NDVI (**a**), NBR (**c**) and NDRE1 (**e**) and with double logistic fitting as described by NDVI (**b**), NBR (**d**) and NDRE1 (**f**), both applied on the vegetation pixels of the five studied areas: Canal de Brienne (olive), Urban Canal de Midi (cyan), Peri-Urban Canal de Midi (green), J. Guesde (magenta) and F. Verdier (red). Black dashed vertical lines indicate DoY 170, 205 and 270 corresponding to the start dates of the two intra-annual phenological disturbance periods and the end of the second one respectively.

Table 4. Mean of the annual phenological dynamics criteria on D-L fitted phenological curves for NDVI, NBR and NDRE1 and for the five studied areas. Standard deviations are indicated within brackets.

NDVI	**SOS20 (DoY)**	**SOS50**	**PS90$_S$**	**PS90$_E$**	**EOS50 (DoY)**	**VI_{max} (VI)**	**Green$_{period}$ (%)**
Brienne	90 (8)	103 (5)	125 (4)	224 (14)	285 (11)	0.87 (0.05)	83 (6)
MiDi Int	92 (5)	106 (4)	128 (8)	225 (16)	284 (12)	0.85 (0.03)	81 (3)
MiDi Ext	95 (2)	108 (3)	128 (2)	247 (12)	293 (6)	0.88 (0.02)	85 (2)
JGuesde	94 (15)	109 (13)	134 (17)	237 (26)	283 (24)	0.76 (0.10)	73 (11)
FVerdier	91 (10)	103 (11)	130 (19)	224 (20)	283 (18)	0.83 (0.09)	78 (9)
NBR	**SOS20 (DoY)**	**SOS50**	**PS90$_S$**	**PS90$_E$**	**EOS50 (DoY)**	**VI_{max} (VI)**	**Green$_{period}$ (%)**
Brienne	94 (2)	105 (2)	125 (7)	276 (14)	308 (10)	0.67 (0.06)	66 (6)
MiDi Int	94 (2)	106 (3)	127 (5)	268 (13)	309 (7)	0.63 (0.05)	62 (5)
MiDi Ext	95 (2)	108 (3)	128 (3)	278 (10)	310 (5)	0.70 (0.02)	69 (2)
JGuesde	92 (5)	108 (6)	136 (17)	276 (26)	308 (16)	0.56 (0.14)	55 (15)
FVerdier	93 (4)	104 (3)	125 (7)	249 (29)	296 (23)	0.58 (0.12)	56 (12)
NDRE1	**SOS20 (DoY)**	**SOS50**	**PS90$_S$**	**PS90$_E$**	**EOS50 (DoY)**	**VI_{max} (VI)**	**Green$_{period}$ (%)**
Brienne	90 (4)	108 (4)	169 (25)	196 (2)	240 (12)	0.60 (0.03)	48 (2)
MiDi Int	96 (4)	112 (5)	158 (25)	197 (4)	245 (15)	0.49 (0.06)	41 (5)
MiDi Ext	96 (4)	113 (4)	142 (19)	207 (16)	261 (17)	0.54 (0.03)	47 (3)
JGuesde	92 (8)	108 (6)	145 (23)	206 (11)	253 (25)	0.48 (0.06)	42 (6)
FVerdier	94 (3)	106 (3)	160 (27)	200 (13)	247 (18)	0.50 (0.08)	42 (6)

On the other hand, criteria such as SOS20, SOS50, PS90$_S$ PS90$_E$ and EOS50 do not allow us to observe differences between the annual phenological dynamics of the different sites as described by NDVI, NBR and NDRE1, see Tables 3 and 4. For any studied site and with any VIs, the start of greenup, indicated by SOS20, is found around DoY 90 with variations between sites of less than one week and standard deviations between a couple of days and a couple of weeks. SOS50, which indicates the midpoint of the greenup period, appears around DoY 105–115 depending on the site, with standard deviations of the same magnitude as the differences. These results are independent of the reconstruction methodology. The position of the peak of maturity, located between PS90$_S$ and PS90$_E$, varies between VIs and reconstruction methodologies. Thus, for NDRE1, independently of the methodology, PS90$_S$ PS90$_E$ criteria predict the peak of maturity to be between DoY 140–170 and DoY 195–210. However, for NDVI and NBR, PS90$_S$ and PS90$_E$ criteria present differences between S-G and D-L time series. While S-G time series for both NDVI and NBR predict PS90$_S$ around DoY 140–150 for any studied area, D-L time series predict earlier greenup of about 20 days (DoY $\approx$ 120–130). This behavior is inverted for PS90$_E$. In this case, D-L time series estimate the starting of senescence around DoY 220–240 for NDVI and 250–280 for NBR, while S-G ones estimate earlier starting of senescence at DoY 200–210 for NDVI and 230–250 for NBR. In addition, whatever the selected VIs, both PS90$_S$ and PS90$_E$ present high variabilities with high standard deviations of around 20 days, especially when differences between the mean values for the different sites are more important. EOS50, indicating the midpoint of senescence, also depends on the observed VI but is independent of the methodology. Thus, for NDVI EOS50 approximately appears on DoY 280–290, for NBR it is around DoY 300–310 and for NDRE1 around DoY 240–260. In the case of NDVI and NBR, the differences of PS90$_S$ and PS90$_E$ between S-G and D-L time series are explained because D-L does not characterize intra-annual sudden drops of VIs, which appear during the maturity period. Hence, we consider that these criteria on S-G time series provide more confident values. In the case of NDRE1, the shape of the phenology curve as described by this VI reduces the differences of PS90$_S$, PS90$_E$ and SOS50 between S-G and D-L methodologies.

4.3.2. Intra-Annual Phenological Disturbance Events Analysis

Only the proposed methodology, with S-G filtering, allows to observe intra-annual phenological disturbance events (defined as periods with anomalous phenological dynamics), while D-L curve fitting method does not (see Figure 9). Thus for NDVI and NDRE1, Figure 9a,e shows a marked disturbance period, characterized by a sharp fall of both VIs [35,61,62], occurring from the end of July (DoY ≈ 205) to September (DoY ≈ 270). This period can be observed on every studied area with a decrease of NDVI and NDRE1 going from around −0.01 NDVI (NDRE1) per week, for London planes from Canal de Brienne, to -0.005 NDVI (NDRE1) per week, for London planes from peri-urban Canal de Midi. Another (less important) intra-annual phenological disturbance period, also characterized by a sharp decrease of VIs appears at the end of June (DoY ≈ 170) on every studied area. Table 5 shows that for NDVI and NDRE1 both, the slope and the area criteria, indicate that London planes from peri-urban Canal de Midi are the less disturbed trees (for NDVI and NDRE1 $SlVI_{205}$ = −0.005 VI/week, and DiffA = 0.010 and 0.007 respectively), while those of Canal de Brienne are more disturbed (for NDVI and NDRE1 $SlVI_{205}$ = −0.008 VI/week and −0.009 VI/week respectively, and DiffA = 0.025 and 0.033 respectively). The rest of areas present phenological disturbance in between.

For NBR, Figure 9c shows a slight phenological disturbance period occurring at the same moment of the one observed in NDVI and NDRE1 (DoY ≈ 205), with a decrease of NBR of −0.004 NBR/week, for London planes from Canal de Brienne, and of −0.002 NBR/week, for London planes from peri-urban Canal de Midi. Thus, NBR seems to be less sensitive to the anomalous phenological dynamics appearing during this period than NDVI or NDRE1. Table 5 shows that for NBR the slope criterion agrees with the results obtained for NDVI and NDRE1. Peri-urban Canal de Midi trees have the less anomalous dynamics, and newly, Canal de Brienne trees show the most anomalous dynamics.

Table 5. Mean of the intra-annual disturbance criteria on S-G filtered phenological curves for NDVI, NBR and NDRE1 and for the five studied areas.

	Site	$SlVI_{t_i}$ (VI/DoY)	Normalized DiffA (VI)
NDVI	Brienne	−0.0011	0.025
	MiDi Int	−0.0010	0.018
	MiDi Ext	−0.0007	0.010
	JGuesde	−0.0008	0.015
	FVerdier	−0.0010	0.019
NBR	Brienne	−0.0005	0.013
	MiDi Int	−0.0004	0.008
	MiDi Ext	−0.0003	0.002
	JGuesde	−0.0003	0.010
	FVerdier	−0.0005	0.011
NDRE1	Brienne	−0.0013	0.033
	MiDi Int	−0.0008	0.015
	MiDi Ext	−0.0007	0.007
	JGuesde	−0.0008	0.019
	FVerdier	−0.0008	0.012

4.4. Climate Factor Influences on Phenological Curves

Figure 10 plots the meteorological data recorded at the Meteopole-Flux station during 2018. These data describe a sudden change of weather condition between DoY 168 and DoY 170 (17–19 June 2018): the daily maximum temperature increases from 22 to 28 °C, and mean global solar radiation from 345 to 515 $W{\cdot}m^{-2}$. Conditions durably remain warm until DoY 224 (12 August 2018) with a maximum daily temperature greater than 30 °C associated to a high radiation forcing. A short heat-wave event is even recorded from 2 to 6 August. In addition, precipitations are low during the period DoY 170–287 leading to a drying of the soil that is more or less rapid and durable depending on the depth of soil layers analyzed. The water content for the near-surface layer (10–50 cm) is very

sensitive to short-term precipitation variation. A rapid decrease from 0.30 to 0.12 $m^3 \cdot m^{-3}$ is noted from DoY 170 followed by a slight increase around DoY 197 due to some rainfall events, and then the water content continues to decrease down to 0.09 $m^3 \cdot m^{-3}$ until the end of the dry period by October. The water content of soil layer 50–100 cm decreases rapidly at the beginning of the dry period (DoY 287) and then stabilizes at around 0.12 $m^3 \cdot m^{-3}$. At this depth, the water content is not sensitive to short-term rainfall events. Finally the deeper soil layer presents a slower dryness following a linear decrease in soil water content from DoY 168 to DoY 280 down to 0.19 $m^3 \cdot m^{-3}$, and then remains unchanged for the rest of the year.

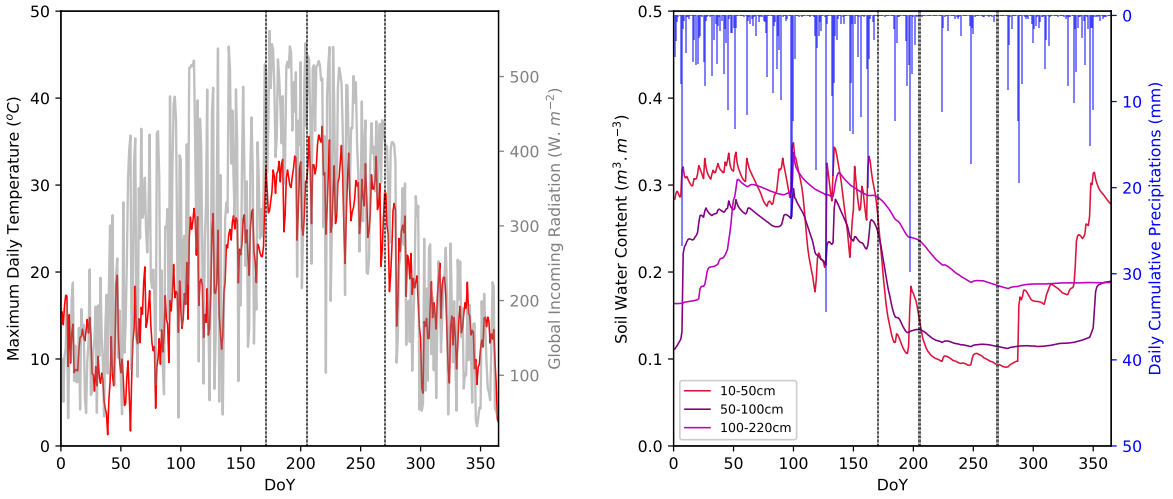

Figure 10. Daily meteorological variables measured at the Centre National de Recherches Meteorologiques (CNRM) de Toulouse: **left**) maximum air temperature (red) and global incoming radiation (gray), **right**) soil water content at three depth levels (red, purple and pink) and precipitations (blue). Black dashed vertical lines indicate DoY 170, 205 and 270 corresponding to the start dates of the two intra-annual phenological disturbance periods and the end of the second one respectively.

Figure 9 gives the phenological curves as described by NDVI, NBR and NDRE1 for the five studied areas together with the vertical dashed lines containing the intra-annual periods of anomalous phenological dynamics (same dashed lines as in Figure 10). These intra-annual phenological disturbance events seems to be linked with the meteorological conditions of the periods: increase in temperatures and total received irradiance and decrease in precipitations and soil water content, see Figure 10.

5. Discussion

5.1. Methodology Hypotheses and Performances

As said in Section 3.1, the proposed method supposes that for VIs time series in urban environments, sudden falls are mainly due to noise induced by registration variability between dates. The magnitude of these sudden drops for the same co-registration error can depend on the spectral contrast between vegetation and background and on the chosen VI used to reconstruct the phenological curve. For these reasons, both the D-L curve fitting and the S-G filtering contain a weighting hypothesis to make reconstructed phenological curves converging to the upper VI envelope and thus correcting this mixed-pixel effect.

The same hypothesis has been proposed for reconstructing VIs in natural environments [45,50,51], where sudden falls in VI time series are considered to be due to atmospheric and cloud cover variability and/or bi-directional effects [51]. Hence, in these cases, the hypothesis grounds on the NIR reflectance decrease when atmospheric transmission is reduced. On the other hand, reflectances in the visible domain increase due to additive path radiance [51]. However, in urban environments, registration

variability between dates appears as the main source of noise due to the important heterogeneity of impervious/natural elements, the 3D structure of cities inducing shadows and the restricted spatial extent of vegetation. This is shown in Figure 8a,b, since the amplitude of the noise depends on the pixel, this noise can not be due to atmospheric effects or the latter are strongly masked by the first.

In this work, classification is based on curve fitting and a statistical condition to avoid pixels with low VI values during the maturity period, see Section 3.1. The main advantage of this classification methodology based on curve fitting is that most of the non-vegetated pixels are excluded for next analysis, see Figure 7. Its drawback is that strongly unhealthy vegetation pixels, with phenologies not following the imposed function, may be considered as non-vegetated ones. In order to improve the classification performances, refined definitions of B_v and B_m depending on VIs, background and vegetation species are further recommended. In addition, to study other species, the bounds of the maturity period may be re-defined following suggestions from Section 3.1.

In the S-G filtering, the weighting hypothesis may hide or reduce possible existing intra-annual phenological disturbance periods, since the filter tends to approach the upper envelope of the time series. However, even if these intra-annual periods are difficult to distinguish from noise, it can be seen in Figure 8 that if these periods are marked enough, they are correctly characterized by the methodology (comparison between green and red curves). The anomalous dynamics of the London planes phenology during a punctual short period may be underestimated, but they are observed.

In addition, the proposed time series reconstruction methodology is semi-automatic since for both steps: curve fitting classification and Savitzky–Golay filtering, the configuration of input parameters is done by the algorithm. Thus, in the minimization needed to time-series fitting, the initial values of the parameters of Equation (1) are directly approximated by the code from the raw time series. For the S-G filtering only two parameters are needed, the size of the smoothing window (m) and the degree of the smoothing polynomial (d). As explained in Section 3.1, the code selects those parameters that lead to smaller errors. Only the range of possible m and d values should be defined, see Section 3.1. Finally, this methodology is generic and appears as applicable on any large-enough group of mono-species urban vegetation, the main limitation being the resolution of the satellite used in the study. The phenology of mono-species grouped trees located in non-urban environments where mixed pixel problems can appear, such as in orchards [75,76] or woodlands/savannas [77–79], might be also studied with the proposed methodology.

5.2. Vegetation Phenology Characterization

Contrary to other works that focus on NDVI time series to describe vegetation phenology [50–52], the proposed methodology enlarges to study other VIs such as: NBR and NDRE1. The use of normalized indices simplifies the quantification of the magnitude of intra-annual phenological disturbance periods, as well as the comparison between VI phenological curves, since the maximum and minimum possible values of the indices are fixed. In addition, analyzing several VIs allows for a more complete characterization of the phenological dynamics since: 1) the different VIs provide information on different vegetation functional and structural variables helping to have a better assessment of vegetation health [37–41] (Table 1) and 2) the sensibility to background, shadows and atmospheric effects varies between VIs.

Among the criteria considered as characterizing the annual phenological dynamics of urban vegetation, VI_{max}, and $\text{Green}_{\text{period}}$ provide the best performances for describing the heterogeneity of the phenological dynamics of the studied sites. While VI_{max} characterizes the annual dynamics with single-date information, that for some VIs can be interpreted as the maximal capacity of vegetation production along the year, $\text{Green}_{\text{period}}$ is not based on a single-date but on the whole maturity period, and is thus less dependent on the number of available images. Taking both of them into account allows to well characterize the VI behavior during the green period. Several potential factors can lead to the obtained phenological dynamics heterogeneity between sites, among them, differences in: 1) The magnitude of the influence of background (including self and cast shadow effects) on

the phenology characterization, 2) the illumination and viewing conditions, 3) the environmental conditions (root space, water availability, temperature differences, etc.), 4) the age of the trees and 5) the orientation of the alignment, etc. To reduce the impact that background and shadows can introduce on the phenology characterization, the pixel classification was performed to discriminate pixels mainly covered by vegetation (where the effects of background are supposed to be lower) from mixed and non-vegetated pixels. Furthermore, the S-G filter applied on vegetation pixels has been also developed to reduce possible remaining influences of mixed pixel effects. In addition, for the five studied areas, buildings are smaller than London planes (except marginal exceptions), and so, no shadows are expected to be cast on the tree top of canopy. The illumination and viewing conditions can be discarded since illumination evolves across the year equally for the five studied sites, and for S-2 used images the viewing angles does not vary, see Section 2. Environmental differences between the studied sites are clear and explained in Section 2.1, for example, the Toulouse town hall indicated that London planes from J. Guesde avenue present health issues due to the long term impact of road works on their root system development and the quality of the soil that has been replaced for this purpose.

The other studied annual criteria: SOS20, SOS50, $PS90_S$, $PS90_E$ and EOS50, based on the characterization of phenological asymmetries [80], are not able to capture the heterogeneities between the different sites. These indicators are based on the date of a given VI amplitude and are very affected by the number of available images, the maximum and minimum VI values and the existence of intra-annual periods of phenological disturbance. Hence, their interpretation when characterizing the phenological dynamics heterogeneity of urban mono-species vegetation is difficult, since differences on start of greenup and senescence are expected to be small. Nevertheless, Vrieling et al. 2018 and Zhou 2019 showed that these criteria are adapted when discriminating different species of vegetation [45,80].

For every tested annual criteria, S-G filtering and D-L fitting methodologies, both on pixels previously classified as vegetation, present similar performances. Since S-G filtering takes into account intra-annual phenological disturbance periods, its description seems to be more accurate even for annual characterizations. However, noise can remain in the S-G reconstructed time series, being a source of error.

Two criteria to quantify the influence of intra-annual phenological disturbance periods (characterized by concavity breaks [35,61,62]) on VIs reconstructed time series have been used: $SlVI_{t_i}$ and DiffA, see Figure 5. While the slope criterion allows us to quantify the disturbance period, very locally in time, by its initial and sudden effect on VI, the area criterion allows to quantify its whole effect on vegetation phenology. The comparison between the reconstructed phenology curve and the straight line has been chosen since the straight line represents the most disturbed possibility for the phenology curve without breaking the concavity/convexity of the time series. Another option would have been to compare, during the intra-annual phenological disturbance period, the S-G reconstructed phenology area to the D-L reconstructed phenology area, see Figure 8. However, the D-L method is based on curve fitting, and thus, the estimated area during the punctual disturbance period will depend on every date of the fitted raw phenology time series. The area criterion should be used carefully, because the same disturbance period can last more or less depending on the used VI. This is not surprising since different VIs provide different information on the vegetation health status and are differently influenced by background. However, intra-annual disturbance events represent slight modifications of phenological curves and then fine spatial resolutions and band widths are important. NDVI, NBR and NDRE1 are calculated at different spatial resolutions: 10 m for NDVI and 20 m for NBR and NDRE1; and band widths: around 100–150 nm for NDVI and NBR and 15 nm for NDRE1. Thus, both low spatial resolutions and wide band widths can hide intra-annual details on phenology curves. The spatial resolution and band widths of NBR may also explain the difficulty to observe the phenological disturbance period during the first week of August 2018 on NBR time series.

5.3. Meteorological Influences on Intra-Annual Phenological Dynamics

The analysis of the evolution of meteorological conditions during 2018 shows their possible influence on the intra-annual phenological disturbance phases of the London planes that have been identified on the monitoring of NDVI, NBR and NDRE1, see Figures 9 and 10. First, air temperature and vapor pressure deficit are the two environmental parameters that govern stomatal opening and plant transpiration. The rapid change to very high heat conditions can also increase rapidly the vapor pressure deficit, that can hasten the decline of vegetation [81,82]. Thus, several works indicated the "strong statistical association between phenology and temperature" [83–86]. On the other hand, the drop in precipitation and soil water availability limits the capability of trees to uptake water by roots for transpiration [82]. For 2018, there are no measurements available at different points in the city to assess the specific meteorological conditions at the different studied sites. This would allow for a better understanding of the intra-annual phenological dynamic differences between sites, since such as Wang et al. 2016 suggested, presenting VI phenology time series versus temperature cumulative indices, and not versus DoY, allows us to better discriminate phenological dynamics [87]. Despite this lack of multiple meteorological stations, in terms of temperature, data collected over Toulouse in 2004–2005 during the CAPITOUL field campaign [88] allows us to visualize the temperature differences according to urban typologies [89]. During summertime, daytime air temperature differences of 1–2 °C were observed between city center and outskirts. These differences was larger at night up to 3–4 °C. Hence, London planes from Midi Ext are considered to be exposed to lower temperatures than London planes from the city center. On the other hand, precipitations are supposed to not strongly vary from one point to the other of the city (especially taking into account the anticyclonic weather prevailing during the most part of the summer of 2018). Thus, the precipitations measured at Meteo-France can illustrate the precipitations at the studied sites. From this consideration, the soil water content sensors located in a grassland ecosystem at Meteo-France can be interpreted as the maximal soil water contents at the Toulouse city center, where impervious surfaces reduce the soil moisture. This hypothesis is only valid for sites far from canals. Then, when soil water content at Meteo-France is low due to lack of precipitations, it is supposed to also be low in the city center far from water sources.

Finally, for Canal de Brienne, Urban Canal de Midi and Peri-urban Canal de Midi, the trees are planted near a water source in an undisturbed natural soil. Consequently, the roots can develop freely (down to deep soil) and uptake soil water. For J. Guesde Avenue and F. Verdier Avenue, trees are planted in a built-up environment where the ground is disturbed and heterogeneous. The root system has less space to expand, which limits access to water and nutrient supplies [90]. In addition, these trees are less exposed to precipitation due to the limited space of soil in which they are planted. In such conditions, trees may be more sensitive to specific disturbance events.

6. Conclusions

This work proposes a new methodology that enables the monitoring of urban tree vegetation phenological dynamics from Sentinel-2 VIs time series reconstruction. First, a pixel by pixel curve fitting classification was performed, based on the hypothesis that healthy vegetation phenology follows a given fixed annual behavior. This allows us to discriminate vegetation, mixed and non-vegetation pixels. Then, on vegetation pixels, a Savitzky–Golay filter is applied to reduce induced noise mainly due to registration variability between dates. This methodology does not describe the phenology curve with a fixed function. So that, with the appropriate criteria, it allows us to characterize annual and intra-annual vegetation phenological dynamics for groups of mono-species urban trees.

In this article, London planes located at five sites with different environmental conditions have been studied during a single year (2018). From one side, VI_{max} and $\text{Green}_{\text{period}}$ criteria show the phenology heterogeneity existing between London planes located at the different sites. However, from another side, criteria based on the date of a given VI amplitude such as SOS20, do not appear to be adapted to illustrate this heterogeneity.

The ability of the proposed methodology to detect the existence of intra-annual phenological disturbance events, that may be linked to environmental conditions, is also shown. Two intra-annual periods of anomalous phenological dynamics were detected during summer. Their influence on the phenological curves has been quantified with two different criteria: SlVI measuring the negative VI time series slope at the beginning of the disturbance period, and DiffA measuring the lose of VI area due to the disturbance event. Furthermore, these phenological disturbance periods have been related to summer meteorological conditions.

Future steps will focus on multi-year studies, for which annual criteria are expected to show differences between phenological curves from one year to another. Combined with meteorological data and field campaigns, these differences would be linked to different yearly meteorological conditions, diseases, pests, pollutants, climate change, etc. Furthermore, the proposed methodology is applicable to single-season deciduous vegetation. However, for evergreen and double-season vegetation (as it appears on tropical climates) the curve fitting classification step should be adapted [52,91]. Finally, the methodology should be tested for different satellites. The new mission VENμS with a spatial resolution of 10 m with all its bands (400–900 nm), and with a revisit time of 2 days appears as a good candidate.

Author Contributions: Conceptualization, C.G.-B., K.A. and X.B.; methodology, C.G.-B., K.A. and X.B.; software, C.G.-B.; formal analysis, C.G.-B.; investigation, C.G.-B.; resources, A.L.; writing—original draft preparation, C.G.-B.; writing—review and editing, C.G.-B., K.A., A.L. and X.B.; funding acquisition, K.A. and X.B. All authors have read and agreed to the published version of the manuscript.

Funding: This research was funded by ONERA contract number 30221001F—2019. The APC was funded by ONERA DOTA.

Acknowledgments: The authors wish to thank the THEIA platform for providing the needed Sentinel-2 processed images (Level 2A). They also wish to thank Meteo-France for providing the meteorological data used in this article. The authors want to thank the administrative office of "Services des espaces verts" of the Toulouse town hall for stimulating discussions. Finally, the authors want to thank ONERA for funding this research.

Conflicts of Interest: The authors declare no conflict of interest.

Appendix A. Sentinel-2 Spectral and Spatial Configuration

Table A1. Spectral and spatial configuration of Sentinel-2.

Sentinel-2 Band	Wavelength	Spatial Resolution
Band 1 - Blue 1	433–453 nm	60 m
Band 2 - Blue 2	458–523 nm	10 m
Band 3 - Green	543–578 nm	
Band 4 - Red 1	650–680 nm	
Band 5 - Red 2	698–713 nm	20 m
Band 6 - Red 3	733–748 nm	
Band 7 - Red 4	773-793 nm	
Band 8 - NIR 1	785–900 nm	10 m
Band 8a - NIR 2	855–875 nm	20 m
Band 9 - NIR 3	935–955 nm	60 m
Band 10 - CIRRUS	1360–1390 nm	
Band 11 - SWIR 1	1565–1655 nm	20 m
Band 12 - SWIR 2	2100–2280 nm	

References

1. Hassan, A.; Lee, H. Toward the sustainable development of urban areas: An overview of global trends in trials and policies. *Land Use Policy* **2015**, *48*, 199–212. [CrossRef]
2. Manning, W. Plants in urban ecosystems: Essential role of urban forests in urban metabolism and succession toward sustainability. *Int. J. Sustain. Dev. World Ecol.* **2008**, *15*, 362–370. [CrossRef]
3. Alexandre, F. The role of vegetation in the urban policies of european cities in the age of the sustainable city. *Eur. Spat. Res. Policy* **2013**, *20*, 11–26. [CrossRef]
4. Vos, P.; Maiheu, B.; Vankerkom, J.; Janssen, S. Improving local air quality in cities: To tree or not to tree? *Environ. Pollut.* **2013**, *183*, 113–122. [CrossRef] [PubMed]
5. Alavipanah, S.; Wegmann, M.; Qureshi, S.; Weng, Q.; Koellner, T. The role of vegetation in mitigating urban land surface temperatures: A case study of Munich, Germany during the warm season. *Sustainability* **2015**, *7*, 4689–4706. [CrossRef]
6. Chaturvedi, A.; Kamble, R.; Patil, N.; Chatuverdi, A. City-forest relationship in Nagpur: One of the greenest cities of India. *Urban Ofrestry Urban Green.* **2013**, *12*, 79–87. [CrossRef]
7. Salbitano, F.; Borelli, S.; Conigliaro, M.; Chen, Y. *Guidelines on Urban and Peri-Urban Forestry*; Technical report; Food and Agricultural Organization of the United Nations: Rome, Italy, 2016; pp.1–172
8. McPherson, E.G.; van Doorn, N.; de Goede, J. Structure, function and value of street trees in California, USA. *Urban For. Urban Green.* **2016**, *17*, 104–115. [CrossRef]
9. Rol-Tanguy, F.; Alba, D.; Dragoni, M.; Minassian, H.T.; Blancot, C. *Essai de Bilan sur le Developpement des Arbres D'Alignement dans Paris*; Technical report; Atelier Parisien d'Urbanisme (APUR): Paris, France, 2010; pp. 1–76.
10. Grimm, N.; Faeth, S.; Golubiewski, N.; Redman, C.; Wu, J.; Bai, X.; Briggs, J. Global change and the ecology of cities. *Science* **2008**, *319*, 756–760. [CrossRef]
11. Salinitro, M.; Alessandrini, A.; Zappi, A.; Tassoni, A. Impact of climate change and urban development on the flora of a southern European city: Analysis of biodiversity change over a 120-year period. *Sci. Rep.* **2019**, *9*, 9464. [CrossRef]
12. Nowak, D. Improving city forests through assessment, modelling and monitoring. *Unasylva* **2018**, *69*, 30–36.
13. Cumming, A.; Galvin, M.; Rabaglia, M.; Cumming, J.; Twardus, D. Forest health monitoring protocol applied to roadside trees in Maryland. *J. Arboric.* **2001**, *27*, 126–138.
14. Ouerghemmi, W.; Gadal, S.; Mozgeris, G. Urban vegetation mapping using hyperspectral imagery and spectral library. In Proceedings of the IEEE International Geoscience and Remote Sensing Symposium (IGARSS), Valencia, Spain, 23–27 July 2018; pp. 1632–1635.
15. Feng, Q.; Liu, J.; Gong, J. UAV remote sensing for urban vegetation mapping using random forest and texture analysis. *Remote Sens.* **2015**, *7*, 1074–1094. [CrossRef]
16. Hashim, H.; Latif, Z.A.; Adnan, N.A. Urban vegetation classification with NDVI thresold value method with very high resolution (VHR) PLEIADES Imagery. *Int. Arch. Photogramm. Remote Sens. Spat. Inf. Sci.* **2019**, *XLII-4*, 237–240. [CrossRef]
17. Mathieu, R.; Aryal, J.; Chong, A. Object-based classification of Ikonos imagery for mapping large-scale vegetation communities in urban areas. *Sensors* **2007**, *7*, 2860–2880. [CrossRef]
18. Tigges, J.; Lakes, T.; Hostert, P. Urban vegetation classification: Benefits of multitemporal RapidEye satellite data. *Remote Sens. Environ.* **2013**, *136*, 66–75. [CrossRef]
19. Wen, D.; Huang, X.; Liu, H.; Liao, W.; Zhang, L. Semantic classification of urban trees using very high resolution satellite imagery. *IEEE J. Sel. Top. Appl. Earth Obs. Remote Sens.* **2017**, *10*, 1413–1424. [CrossRef]
20. Degerickx, J.; Roberts, D.; McFadden, J.; Hermy, M.; Somers, B. Urban tree health assessment using airborne hyperspectral and LiDAR imagery. *Int. J. Appl. Earth Obs. Geoinf.* **2018**, *73*, 26–38. [CrossRef]
21. Sari, N.; Kushardono, D. Quality analysis of single tree object with obia and vegetation index from lapan surveillance aircraft multispectral data in urban area. *Geoplan. J. Geomat. Plan.* **2016**, *3*, 93–106. [CrossRef]
22. Xiao, Q.; McPherson, E. Tree health mapping with multispectral remote sensing data at UC Davis, California. *Urban Ecosyst.* **2005**, *8*, 349–361. [CrossRef]
23. Cârlan, I.; Mihai, B.A.; Nistor, C.; GroBe-Stoltenberg, A. Identifying urban vegetation stress factors based on open access remote sensing imagery and field observations. *Ecol. Inform.* **2020**, *55*, 101032. [CrossRef]

24. Li, Y.; Yu, H.; Wang, Y.; Wu, J.; Yang, L. Classification of urban vegetation based on unmanned aerial vehicle reconstruction point cloud and image. *Remote Sens. Land Resour.* **2019**, *31*, 149–155.
25. Jarocińska, A.; Bialczak, M.; Slawik, L. Application of aerial hyperspectral images in monitoring tree biophysical parameters in urban areas. *Misc. Geogr.* **2018**, *22*, 56–62. [CrossRef]
26. Delegido, J.; Wittenberghe, S.V.; Verrelst, J.; Ortiz, V.; Veroustraete, F.; Valcke, R.; Samson, R.; Rivera, J.P.; Tenjo, C.; Moreno, J. Chlorophyll content mapping of urban vegetation in the city of Valencia based on the hyperspectral NAOC index. *Ecol. Indic.* **2014**, *40*, 34–42, doi10.1016/j.ecolind.2014.01.002. [CrossRef]
27. Jensen, R.; Hardin, P.; Bekker, M.; Farnes, D.; Lulla, V.; Hardin, A. Modeling urban leaf area index with AISA+ hyperspectral data. *Appl. Geogr.* **2009**, *29*, 320–332. [CrossRef]
28. Zhang, W.; Zhang, X.; Li, L.; Zhang, Z. Urban forest in Jinan city: Distribution, classification and ecological significance. *Catena* **2007**, *69*, 44–50. [CrossRef]
29. Zhang, X.; Friedl, M.A.; Schaaf, C.B.; Strahler, A.H.; Hodges, J.C.F.; Gao, F.; Reed, B.C.; Huete, A. Monitoring vegetation phenology using MODIS. *Remote Sens. Environ.* **2003**, *84*, 471–475. [CrossRef]
30. Seyednasrollah, B.; Young, A.; Hufkens, K.; Milliman, T.; Friedl, M.; Frolking, S.; Richardson, A. Tracking vegetation phenology across diverse biomes using version 2.0 of the PhenoCam Dataset. *Sci. Data* **2019**, *6*, 222. [CrossRef]
31. Lu, H.; Raupach, M.; McVicar, T.; Barret, D. Decomposition of vegetation cover into woody and herbaceous components using AVHRR NDVI time series. *Remote Sens. Environ.* **2003**, *86*, 1–18. [CrossRef]
32. Hill, M.; Donald, G. Estimating spatio-temporal patterns of agricultural productivity in fragmented landscapes using AVHRR NDVI time series. *Remote Sens. Environ.* **2003**, *84*, 367–384. [CrossRef]
33. Jacquin, A.; Sheeren, D.; Lacombe, J.P. Vegetation cover degradation assessment in Madagascar savanna based on trend analysis of MODIS NDVI time series. *Int. J. Appl. Earth Obs. Geoinf.* **2010**, *12*, S3–S10. [CrossRef]
34. Eckert, S.; Husler, F.; Liniger, H.; Hodel, E. Trend analysis of MODIS NDVI time series for detecting land degradation and regeneration in Mongolia. *J. Arid. Environ.* **2015**, *113*, 16–28. [CrossRef]
35. Liu, Y.; Hill, M.; Zhang, X.; Wang, Z.; Richardson, A.; Hufkens, K.; Filippa, G.; Baldocchi, D.D.; Ma, S.; Verfaillie, J.; et al. Using data from Landsat, MODIS, VIIRS and PhenoCams to monitor the phenology of California oak/grass savanna and open grassland across spatial scales. *Agric. For. Meteorol.* **2017**, *237–238*, 311–325. [CrossRef]
36. Vrieling, A.; Skidmore, A.K.; Wang, T.; Meroni, M.; Ens, B.J.; Oosterbeek, K.; O'Connor, B.; Darvishzadeh, R.; Heurich, M.; Shepherd, A.; et al. Spatially detailed retrievals of spring phenology from single-season high-resolution image time series. *Int. J. Appl. Earth Obs. Geoinf.* **2017**, *59*, 19–30. [CrossRef]
37. Kuusk, A. Monitoring of vegetation parameters on large areas by the inversion of a canopy reflectance model. *Int. J. Remote Sens.* **1998**, *19*, 2893–2905. [CrossRef]
38. Baret, F.; Buis, S. Estimating Canopy Characteristics from Remote Sensing Observations: Review of Methods and Associated Problems. In *Advances in Land Remote Sensing*; Liang, S., Ed.; Springer: Dordrecht, The Netherlands, 2008; pp. 171–200.
39. Jacquemoud, S.; Verhoef, W.; Baret, F.; Bacour, C.; Zarco-Tejada, P.; Asner, G.; Francois, C.; Ustin, S. PROSPECT + SAIL models: A review of use for vegetation characterization. *Remote Sens. Environ.* **2009**, *113*, S56–S66. [CrossRef]
40. Verrelst, J.; Camps-Valls, G.; Muñoz-Marí, J.; dn F. Veroustraete, J.R.; Clevers, J.; Moreno, J. Optical remote sensing and the retrieval of terrestril vegetation bio-geophysical properties—A review. *Isprs J. Photogramm. Remote Sens.* **2015**, *108*, 273–290. [CrossRef]
41. Morcillo-Pallarés, P.; Rivera-Caicedo, J.; Belda, S.; Grave, C.D.; Burriel, H.; Moreno, J.; Verrelst, J. Quantifying the robustness of vegetation indices through global sensitivity analysis of homogeneous and forest leaf-canopy radiattive transfer models. *Remote Sens.* **2019**, *11*, 2418. [CrossRef]
42. Thenkabail, P.; Mariotto, I.; Gumma, M.; Middleton, E.; Landis, D.; Huemmrich, K. Selection of hyperspectral narrowbands and composition of hyperspectral twoband vegetation indices for biophysical characterization and discrimination of crop types using field reflectance and Hyperion/EO-1 data. *IEEE J. Sel. Top. Appl. Earth Obs. Remote Sens.* **2013**, *6*, 427–439. [CrossRef]
43. Guyot, G.; Guyon, D.; Riom, J. Factors affecting the spectral response of forest canopies: A review. *Geocarto Int.* **1989**, *4*, 3–18. [CrossRef]

44. Zhang, X.; Friedl, M.A.H.; Strahler, C.S.; Hodges, J.; Gao, F.; Reed, B.; Huete, A. Monitoring vegetation phenology using MODIS. *Remote Sens. Environ.* **2003**, *84*, 471–475. [CrossRef]
45. Vrieling, A.; Meroni, M.; Darvishzadeh, R.; Skidmore, A.; Wang, T.; Zurita-Milla, R.; Oosterbeek, K.; O'Connor, B.; Paganini, M. Vegetation phenology from Sentinel-2 and fields cameras for a Dutch barrier island. *Remote Sens. Environ.* **2018**, *215*, 517–529. [CrossRef]
46. Jakubauskas, M.; Legates, D.; Kastens, J. Harmonic analysis of time-series AVHRR NDVI data. *Photogramm. Eng. Remote Sens.* **2001**, *67*, 461–470.
47. Geerken, R.; Zaitchik, B.; Evans, J. Classifying rangeland vegetation type and coverage from NDVI time series using Fourier Filtered Cycle Similarity. *Int. J. Remote Sens.* **2005**, *26*, 5535–5554. [CrossRef]
48. Viovy, N.; Arino, O.; Belward, A. The Best Index Slope Extraction (BISE): A method for reducing noise in NDVI time-series. *Int. J. Remote Sens.* **1992**, *13*, 1585–1590. [CrossRef]
49. Lovell, J.; Graetz, R. Filtering pathfinder AVHRR land NDVI data for Australia. *Int. J. Remote Sens.* **2001**, *22*, 2649–2654. [CrossRef]
50. Chen, J.; Jonsson, P.; Tamura, M.; Gu, Z.; Matsushita, B.; Eklundh, L. A simple method for reconstructing a high-quality NDVI time-series data set based on the Savitzky-Golay filter. *Remote Sens. Environ.* **2004**, *91*, 332–344. [CrossRef]
51. Beck, P.; Atzberger, C.; Hogda, K.; Johansen, B.; Skidmore, A.K. Improved monitoring of vegetation dynamics at very high latitudes: A new mothod using MODIS NDVI. *Remote Sens. Environ.* **2006**, *100*, 321–334. [CrossRef]
52. Yang, Y.; Luo, J.; Huang, Q.; Wu, W.; Sun, Y. Weighted double-logistic function fitting method for reconstructing the high-quality Sentinel-2 NDVI time series data set. *Remote Sens.* **2019**, *11*, 2342. [CrossRef]
53. Roerink, G.; Menenti, M.; Verhoef, W. Reconstructing cloudfree NDVI composites using Fourier analysis of time series. *Int. J. Remote Sens.* **2010**, *21*, 1911–1917. [CrossRef]
54. Sellers, P.; Tucker, C.; Collatz, G.; Los, S.; Justice, C.; Dazlich, D.; Randall, D. A global 1° by 1° NDVI data set for climate studies. Part 2: The generation of global fields of terrestrial biophysical parameters from the NDVI. *Int. J. Remote Sens.* **1994**, *15*, 3519–3545. [CrossRef]
55. Li, X.; Zhou, Y.; Meng, L.; Asrar, G.R.; Lu, C.; Wu, Q. A dataset of 30 m annual vegetation phenology indicators (1985–2015) in urban areas of the conterminous United States. *Earth Syst. Sci. Data* **2019**, *11*, 881–894. [CrossRef]
56. Qiu, T.; Song, C.; Li, J. Impacts of Urbanization on Vegetation Phenology over the Past Three Decades in Shanghai, China. *Remote Sens.* **2017**, *9*, 970. [CrossRef]
57. Li, F.; Song, G.; Liujun, Z.; Yanan, Z.; Di, L. Urban vegetation phenology analysis using high spatio-temporal NDVI time series. *Urban For. Urban Green.* **2017**, *25*, 43–57. [CrossRef]
58. Ferrier, P.; Crebassol, P.; Dedieu, G.; Hagolle, O.; Meygret, A.; Tinto, F.; Yaniv, Y.; Herscovitz, J. VENμS (Vegetation and Environment monitoring on a New MicroSatellite). In Proceedings of the IEEE International Geoscience and Remote Sensing Symposium, Honolulu, Hi, USA, 25–30 July 2010.
59. Panconesi, A. Canker stain of plane trees: A serious danger to urban plantings in europe. *J. Plant Pathol.* **1999**, *81*, 3–15.
60. Anselmi, N.; Cardin, L.; Nicolotti, G. Plane decline in European and Mediterranean countries: Associated pests and their interactions. *Eppo Bull.* **1994**, *24*, 159–171. [CrossRef]
61. Gouveia, C.; Trigo, R.; DaCamara, C. Drought and vegetation stress monitoring in portugal using satellite data. *Nat. Hazards Earth Syst. Sci.* **2009**, *9*, 185–195. [CrossRef]
62. Verbesselt, J.; Hyndman, R.; Zeileis, A.; Culvenor, D. Phenological change detection while accounting for abrupt and gradual trends in satellite image time series. *Remote Sens. Environ.* **2010**, *114*, 2970–2980. [CrossRef]
63. Zhou, D.; Xiao, J.; Bonafoni, S.; Berger, C.; Deilami, K.; Zhou, Y.; Frolking, S.; Yao, R.; Qiao, Z.; Sobrino, J. Satellite remote sensing of surface urban heat islands: Progress, challenges and perspectives. *Remote Sens.* **2019**, *11*, 48. [CrossRef]
64. Clerc, S.; MPC Team. *Sentinel-2 L1C Data Quality Report*; Technical report; ESA: Paris, France, 2020; pp. 1–49.
65. Hawrylo, P.; Bednarz, B.; Wezyk, P.; Szostak, M. Estimating defoliation of scots pine stands using machine learning methods and vegetation indices of Sentinel-2. *Eur. J. Remote Sens.* **2018**, *58*, 194–204. [CrossRef]

66. Rouse, J.; Haas, R.; Schell, J.; Deering, D. Monitoring vegetation systems in the great plains with ERTS. In Proceedings of the Third ERTS Symposium, Washington, DC, USA, 29 October–10 December 1973; pp. 309–317.
67. Kriegler, F.; Malila, W.; Nalepka, R.; Richardson, W. Preprocessing transformations and their effect on multispectral recognition. In Proceedings of the 6th International Symposium on Remote Sensing of Environment, Ann Arbor, MI, USA, 13–16 October 1969; pp. 97–131.
68. Key, C.; Benson, N. *Landscape Assessment: Ground Measure of Severity, the Composite Burn Index; and Remote Sensing of Severity, the Normalized Burn Ratio*; Technical report; USDA Forest Service, Rocky Mountain Research Station: Ogden, UT, USA, 2006; pp. 1–51.
69. Zarco-Tejada, P.; Hornero, A.; Beck, P.; Kattenborn, T.; Kempeneers, P.; Hernández-Clemente, R. Chlorophyll content estimation in an open-canopy conifer forest with Sentinel-2A and hyperspectral imagery in the context of forest decline. *Remote Sens. Environ.* **2019**, *223*, 320–335. [CrossRef]
70. Clevers, J.; Gitelson, A. Remote estimation of crop and grass chlorophyll and nitrogen content using red-edge bands on Sentinel 2 and -3. *Int. J. Appl. Earth Obs. Geoinf.* **2013**, *23*, 344–351. [CrossRef]
71. Gitelson, A.; Merzlyak, M. Spectral reflectance changes associated with autumn senescence of *Aesculus hippocastanum* L. and *Acer platanoides* L. leaves. Spectral features and relation to chlorophyll estimation. *J. Plants Physiol.* **1994**, *143*, 286–292. [CrossRef]
72. Levenberg, K. A method for the solution of certain non-linear problems in least squares. *Q. Appl. Math.* **1944**, *2*, 164–168. [CrossRef]
73. Marquardt, D. An algorithm for least-squares estimation of nonlinear parameters. *Siam J. Appl. Math.* **1963**, *11*, 431–441. [CrossRef]
74. Virtanen, P.; Gommers, R.; Oliphant, T.E.; Haberland, M.; Reddy, T.; Cournapeau, D.; Burovski, E.; Peterson, P.; Weckesser, W.; Bright, J.; et al. SciPy 1.0—Fundamental Algorithms for Scientific Computing in Python. *arXiv* **2019**, arXiv:1907.10121.
75. Salgadoe, A.S.A.; Robson, A.J.; Lamb, D.W.; Dann, E.K.; Searle, C. Quantifying the severity of Phytophthora root rot disease in avocado trees using image analysis. *Remote Sens.* **2018**, *10*, 226. [CrossRef]
76. Bellvert, J.; Adeline, K.; Baram, S.; Pierce, L.; Sanden, B.L.; Smart, D.R. Monitoring crop evapotranspiration and crop coefficients over an almond and pistachio orchard throughout remote sensing. *Remote Sens.* **2018**, *10*, 2001. [CrossRef]
77. Joffre, R.; Lacaze, B. Estimating tree density in oak savanna-like "dehesa" of southern Spain from SPOT data. *Int. J. Remote Sens.* **1993**, *14*, 685–697. [CrossRef]
78. Joffre, R.; Rambal, S.; Ratte, J. The dehesa system of southern Spain and Portugal as a natural ecosystem mimic. *Agrofor. Syst.* **1999**, *45*, 57–79. [CrossRef]
79. Miraglio, T.; Adeline, K.; Huesca, M.; Ustin, S.; Briottet, X. Monitoring LAI, chlorophylls, and carotenoids content of a woodland savanna using hyperspectral imagery and 3D radiative transfer modeling. *Remote Sens.* **2019**, *12*, 28. [CrossRef]
80. Zhou, Y. Asymmetric behavior of vegetation seasonal growth and the climatic cause: Evidence from long-term NDVI dataset in northeast China. *Remote Sens.* **2019**, *11*, 2107. [CrossRef]
81. Will, R.; Wilson, S.; Zou, C.; Hennessey, T. Increased vapor pressure deficit due to higher temperature leads to greater transpiration and faster mortality during drought for tree seedlings common to the forest–grassland ecotone. *New Phytol. Trust.* **2013**, *200*, 366–374. [CrossRef] [PubMed]
82. Gillner, S.; Brauning, A.; Roloff, A. Dendrochronological analysis of urban trees: Climatic response and impact of drought on frequently used tree species. *Trees* **2014**, *28*, 1079–1093. [CrossRef]
83. Jochner, S.; Menzel, A. Urban phenological studies—Past, present future. *Environ. Pollut.* **2015**, *203*, 250–261. [CrossRef]
84. Menzel, A.; Sparks, T.; Estrella, N.; Koch, E.; Aasa, A.; Ahas, R.; Alm-Kübler, K.; Bissolli, P.; Braslavska, O.; Briede, A.; et al. European phenological response to climate change matches the warming pattern. *Glob. Chang. Biol.* **2006**, *12*, 1969–1976. [CrossRef]
85. Wielgolaski, F. Phenological modifications in plants by various edaphic factors. *Int. J. Biometeorol.* **2001**, *45*, 196–202. [CrossRef]
86. Wielgolaski, F. Starting dates and basic temperatures in phenological observations of plants. *Int. J. Biometeorol.* **1999**, *42*, 158–168. [CrossRef]

87. Wang, R.; Cherkauer, K.; Bowling., L. Corn response to climate stress detected with satellite-based NDVI time series. *Remote Sens.* **2016**, *8*, 269. [CrossRef]
88. Masson, V.; Gomes, L.; Pigeon, G.; Liousse, C.; Pont, V.; Lagouarde, J.P.; Salmond, J.; Oke, T.; Hidalgo, J.; Legain, D.; et al. The Canopy and Aerosol Particles Interactions in TOulouse Urban Layer (CAPITOUL) experiment. *Meteorol. Atmos. Phys.* **2008**, *102*, 135. [CrossRef]
89. Houet, T.; Pigeon, G. Mapping urban climate zones and quantifying climate behaviors—An application on Toulouse urban area (France). *Environ. Pollut.* **2011**, *159*, 2180–2192. [CrossRef]
90. Krizek, D.; Dubik, S. Influence of water stress and restricted root volume on growth and development of urban trees. *J. Arboric.* **1987**, *13*, 47–55.
91. Hmimina, G.; Dufrêne, E.; Pontailler, J.Y.; Delpierre, N.; Aubinet, M.; Caquet, B.; de Grandcourt, A.; Burban, B.; Flechard, C.; Granier, A.; et al. Evaluation of the potential of MODIS satellite data to predict vegetation phenology in different biomes: An investigation using ground-based NDVI measurements. *Remote Sens. Environ.* **2013**, *132*, 145–158. [CrossRef]